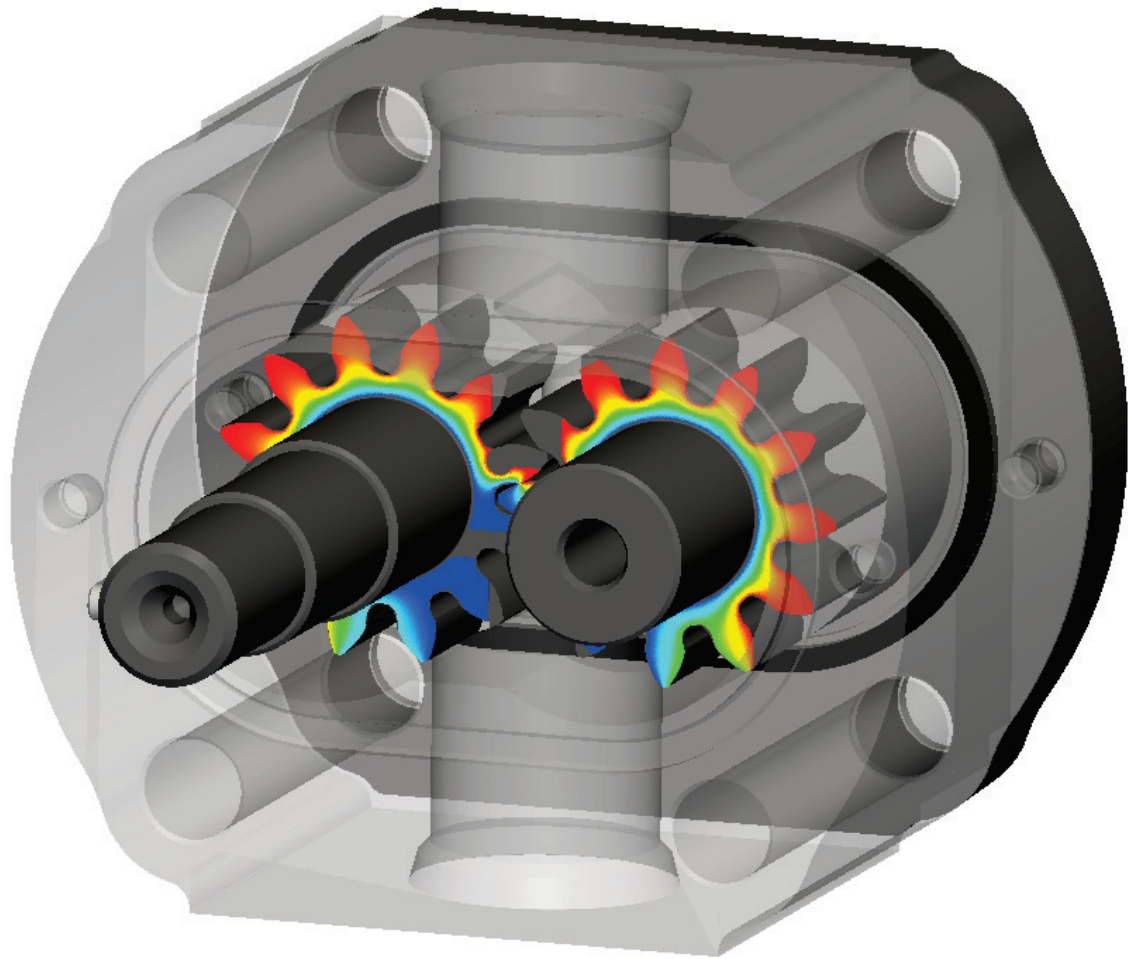


# CHALMERS



## Numerical analysis of the lubricant gap in external gear pumps considering micro level surface features

*Master's Thesis in Solid and Fluid Mechanics*

JOHAN MAGNUSSON

Department of Applied Mechanics  
CHALMERS UNIVERSITY OF TECHNOLOGY  
Gothenburg, Sweden 2011  
Master's Thesis 2011:49



Numerical analysis of the lubricant gap in external gear pumps  
considering micro level surface features

Master's Thesis in Solid and Fluid Mechanics  
JOHAN MAGNUSSON

Department of Applied Mechanics  
*Division of Fluid Dynamics*  
CHALMERS UNIVERSITY OF TECHNOLOGY  
Gothenburg, Sweden 2011

Numerical analysis of the lubricant gap in external gear pumps considering micro level surface features

JOHAN MAGNUSSON

©JOHAN MAGNUSSON, 2011

Master's Thesis 2011:49

ISSN 1652-8557

Department of Applied Mechanics

Division of Fluid Dynamics

Chalmers University of Technology

SE-412 96 Gothenburg

Sweden

Telephone: + 46 (0)31-772 1000

Cover:

External gear pump and the lubricating gap between the gears lateral side and bushing.

Chalmers Reproservice

Gothenburg, Sweden 2011

Numerical analysis of the lubricant gap in external gear pumps considering micro level surface features

Master's Thesis in Solid and Fluid Mechanics

JOHAN MAGNUSSON

Department of Applied Mechanics

Division of Fluid Dynamics

Chalmers University of Technology

### Abstract

The design procedure has made the manufactures through experience aware that the tolerances in gear machines plays a significant influence on the system. In literature there is only a few studies that investigates the phenomena of the geometrical micro details. This due to the complexity of the problem since it involves multiple domains and scales. This work will prove how it is possible to investigate the problem involving micro level details and the goal has been to study the effects with the aim of quantifying and proving the impact of a chamfer on the gears lateral side.

The work has been performed by coupling the tooth space pressures solved by HYGESim (Hydraulic Gear machines Simulator) with a numerical solver developed in an OpenFOAM environment. The simulations are carried out by solving Reynolds equations which has been proven to give accurate solutions to problems involving fluid films. Simulations involving both with and without the balancing squeeze term has been performed.

Two different chamfers has been compared to a case without a chamfer at a fixed and constant gap height. The different cases are compared to each other by first separation the terms in Reynolds equation and then comparing the leakages to the drain and the power losses. It was found out that chamfer generates translational squeeze effects, which makes this study first of its kind. It was also found out that the generated hydrodynamic effects tends to increase with an increased chamfer. When it comes to the leakages, the chamfer has a positive effect, i.e decreased leakages. When comparing the power losses for one of the chamfers, the smaller one gives decreased losses while the bigger one generates increased losses.

Simulations are also performed with the normal squeeze term taken into account, this to balance the generated forces by tilting the bushing. The results indicate that the hydrodynamic pressures generated to balance the bushing mainly originate from the tilt and not from the chamfer, even though the chamfer tends to decrease the maximum generated pressure and decreasing the tilt constant,  $t$ .

Keywords: External gear pump, lateral, bushing, CFD, openfoam, balance, gsl, reynolds equation, leakages, power losses



# Contents

<b>Abstract</b>	<b>I</b>
<b>Table of Contents</b>	<b>III</b>
<b>Preface</b>	<b>XI</b>
<b>1 Introduction</b>	<b>1</b>
1.1 External gear pump overview	1
1.2 Background and state-of-the-art	4
1.3 Purpose	6
1.4 Sustainable development	6
<b>2 Theoretical complementary</b>	<b>8</b>
2.1 Reynolds Equation	8
2.1.1 Navier-Stokes equations	8
2.1.2 Continuity equation	10
2.1.3 Physical meaning of different terms in Reynolds equation	12
2.2 Axial balance	12
2.3 Gap height calculation	14
2.4 Lateral leakages derivation	14
2.5 Shear stress derivation	16
2.6 Power losses	17
<b>3 Modelling approach</b>	<b>17</b>
3.1 Mesh generation	18
3.1.1 Mesh rotation	18
3.2 Boundary conditions	21
3.3 OpenFOAM solver and implementations	23
3.3.1 Solving Reynolds Equation	23
3.3.2 Creation of gears lateral profile	24
3.3.3 Implementation of micro level surface features in OpenFOAM	25
3.3.4 Numerical solver settings in OpenFOAM	26
3.3.5 Balancing procedure	27
3.3.6 Separation of forces	30
3.3.7 Leakage calculation	31
3.3.8 Shear stress calculation and power losses	31
3.3.9 Initial conditions and geometry dimensions	32
<b>4 Results</b>	<b>34</b>
4.1 Pressure distribution and sources of hydrodynamic pressure generation	35
4.2 Leakage comparison	38
4.2.1 Leakage verification	38
4.2.2 Drain leakage comparison	40
4.3 Shear stress and power losses	41
4.4 Pressure distribution generated by fully balanced gear	46
<b>5 Summary and Conclusions</b>	<b>49</b>
5.1 Fixed gap height, leakages and powerlosses	50
5.2 Fully balanced gear	50

**6 Future work**

**51**

**References**

**53**



# List of Figures

1.1	Classification of displacement machines.[1]	2
1.2	External gear pump, CASAPPA PLP20 11.2 Standard	3
1.3	Exploded view of an external gear pump, CASAPPA PLP20 11.2 Standard.	3
1.4	Front view of the bushing, high pressure port at the top and low pressure port at the lower part. Low pressure connected to the drain.	3
1.5	Back side of the bushing, high pressure port connected to the back side to generate a balancing force. Low pressure port connected to the drain at the lower part.	3
1.6	Meshing process through an external gear pump, basic principles.	4
1.9	Structure of the combined HYGESim model with presented flux between the different modules.	5
1.7	Transparent view of an external gear pump.	7
1.8	Transparent view of an external gear pump describing location of the lubrication gap, between the gears and the bushing.	7
2.1	Coordinate system over a lubrication gap, where h is the gap height.	8
2.2	The bearing with the different forces and their direction against the bushing.	13
2.3	$F_{TSV}$	13
2.4	$F_{relief\ grooves}$	13
2.5	$F_{gap}$	13
2.6	Sketch over the three datum point at the bearings. Notice the high pressure and low pressure grooves.	15
2.7	Leakages between the tooth space volume and leakages to the drain at the gears lateral side.	15
2.8	Boundary patches where the lateral leakages are calculated, including a zoom of a representing boundary face.	15
3.1	Mesh with boundary layers and refinements made in ANSYS Workbench.	19
3.2	Mesh with the high pressure and low pressure ports. Cells intersecting with the ports are removed.	19
3.3	Non-smoothen surface.	20
3.4	Smooth surface which perfectly follow the geometrical details.	20
3.5	Mesh with 100 $\mu\text{m}$ chamfer at different angular positions.	21
3.6	Boundary patches along the drive and slave gear.	21
3.7	Difference between the two used boundary conditions from HYGESim.	22
3.8	Back side of the bearing, showing the high pressure groove and its start at 118°.	23
3.9	hbFieldMaker	24
3.10	Surface geometry described by a STL file.	25
3.11	Input-file to OpenFOAM, the different columns represent different angles on the complete gears lateral profile. $i$ represents row and $0 \dots \frac{\pi}{4}$ the range of angular position of the nodes.	25
3.12	The schematic solver scheme to calculate the tilt of the bearing and the $\sum F = 0$ .	27
3.13	Separation of the pressure generative effects in the lubricating gap.	31
3.14	Pump characterization curves for varying gap heights, compared with experimental data[2].	34
3.15	Different chamfers compared, assumed to follow the equation of a circle, Equation 3.5.	34

4.1	Pressure distribution without chamfer, fixed gap height of 10 $\mu m$ @ 150 bar, 1000 rpm. . . . .	35
4.2	Pressure distribution with 45 $\mu m$ chamfer, fixed gap height of 10 $\mu m$ @ 150 bar, 1000 rpm. . . . .	35
4.3	Pressure distribution with 100 $\mu m$ chamfer, fixed gap height of 10 $\mu m$ @ 150 bar, 1000 rpm. . . . .	35
4.4	Pressure generation by the Poiseuille effects without chamfer, fixed gap height of 10 $\mu m$ @ 150 bar, 1000 rpm. . . . .	36
4.5	Pressure generation by the Poiseuille effects with a 45 $\mu m$ chamfer, fixed gap height of 10 $\mu m$ @ 150 bar, 1000 rpm. . . . .	36
4.6	Pressure generation by the Poiseuille effects with a 100 $\mu m$ chamfer, fixed gap height of 10 $\mu m$ @ 150 bar, 1000 rpm. . . . .	36
4.7	Hydrodynamic pressure generation without chamfer, fixed gap height of 10 $\mu m$ @ 150 bar, 1000 rpm. . . . .	37
4.8	Hydrodynamic pressure generation with 45 $\mu m$ chamfer, fixed gap height of 10 $\mu m$ @ 150 bar, 1000 rpm. . . . .	37
4.9	Hydrodynamic pressure generation with 100 $\mu m$ chamfer, fixed gap height of 10 $\mu m$ @ 150 bar, 1000 rpm. . . . .	37
4.13	Gap height $h$ according to the solved equation, Equation 3.1. . . . .	37
4.10	Hydrodynamic wedge effects without chamfer, fixed gap height of 10 $\mu m$ @ 150 bar, 1000 rpm. . . . .	38
4.11	Hydrodynamic wedge effects with 45 $\mu m$ chamfer, fixed gap height of 10 $\mu m$ @ 150 bar, 1000 rpm. . . . .	38
4.12	Hydrodynamic wedge effects with 100 $\mu m$ chamfer, fixed gap height of 10 $\mu m$ @ 150 bar, 1000 rpm. . . . .	38
4.14	Translational squeeze effects without chamfer, fixed gap height of 10 $\mu m$ @ 150 bar, 1000 rpm. . . . .	39
4.15	Translational squeeze effects with 45 $\mu m$ chamfer, fixed gap height of 10 $\mu m$ @ 150 bar, 1000 rpm. . . . .	39
4.16	Translational squeeze effects with 100 $\mu m$ chamfer, fixed gap height of 10 $\mu m$ @ 150 bar, 1000 rpm. . . . .	39
4.17	Leakage verification to the drain by comparing a tiny chamfer with a case without a chamfer. . . . .	39
4.18	Leakages to the drain @ 20 bar, 1000 rpm. . . . .	40
4.19	Leakages to the drain @ 80 bar, 1000 rpm. . . . .	40
4.20	Leakages to the drain @ 150 bar, 1000 rpm. . . . .	40
4.21	Leakages to the drain @ 240 bar, 1000 rpm. . . . .	40
4.22	Leakages to the drain @ 150 bar, 200 rpm. . . . .	41
4.23	Leakages to the drain @ 150 bar, 1000 rpm. . . . .	41
4.24	Leakages to the drain @ 150 bar, 1500 rpm. . . . .	41
4.25	Leakages to the drain @ 150 bar, 2500 rpm. . . . .	41
4.26	Shear stresses generated without chamfer, fixed gap height of 10 $\mu m$ @ 150 bar, 1000 rpm. . . . .	42
4.27	Shear stresses generated with 45 $\mu m$ chamfer, fixed gap height of 10 $\mu m$ @ 150 bar, 1000 rpm. . . . .	42
4.28	Shear stresses generated with 100 $\mu m$ chamfer, fixed gap height of 10 $\mu m$ @ 150 bar, 1000 rpm. . . . .	42
4.29	Shear stresses generated without chamfer with a zoom on teeth, fixed gap height of 10 $\mu m$ @ 150 bar, 1000 rpm. . . . .	43

4.30	Shear stresses generated with 45 $\mu m$ chamfer with a zoom on teeth, fixed gap height of 10 $\mu m$ @ 150 bar, 1000 rpm. . . . .	43
4.31	Shear stresses generated with 100 $\mu m$ chamfer with a zoom on teeth, fixed gap height of 10 $\mu m$ @ 150 bar, 1000 rpm. . . . .	43
4.32	Power losses generated in the lubricating gap without chamfer, power losses, P, in W, constant gap height. . . . .	44
4.33	Power losses generated in the lubricating gap with 45 $\mu m$ chamfer, P, in W, constant gap height. . . . .	44
4.34	Power losses generated in the lubricating gap with 100 $\mu m$ chamfer, P, in W, constant gap height. . . . .	44
4.35	Absolute difference in power losses between without and with a 45 $\mu m$ chamfer, P, in W, constant gap height. . . . .	45
4.36	Absolute difference in power losses between without and with a 100 $\mu m$ chamfer, P, in W, constant gap height. . . . .	45
4.37	Difference in power losses between without and with a 45 $\mu m$ chamfer, P, in %, constant gap height. . . . .	45
4.38	Difference in power losses between without and with a 100 $\mu m$ chamfer, P, in %, constant gap height. . . . .	45
4.39	Pressure distribution without chamfer, balanced gear @ 150 bar, 1000 rpm. . . . .	46
4.40	Pressure distribution with a 45 $\mu m$ chamfer, balanced gear @ 150 bar, 1000 rpm. . . . .	46
4.41	Hydrodynamic pressure generation without chamfer, balanced gear @ 150 bar, 1000 rpm. . . . .	47
4.42	Hydrodynamic pressure generation with a 45 $\mu m$ chamfer, balanced gear @ 150 bar, 1000 rpm. . . . .	47
4.43	Normal squeeze pressure generation without chamfer, balanced gear @ 150 bar, 1000 rpm. . . . .	47
4.44	Normal squeeze pressure generation with a 45 $\mu m$ chamfer, balanced gear @ 150 bar, 1000 rpm. . . . .	47
4.45	Translational squeeze pressure generation without chamfer, balanced gear @ 150 bar, 1000 rpm. . . . .	47
4.46	Translational squeeze pressure generation with a 45 $\mu m$ chamfer, balanced gear @ 150 bar, 1000 rpm. . . . .	47
4.47	Physical wedge pressure generation without chamfer, balanced gear @ 150 bar, 1000 rpm. . . . .	48
4.48	Physical wedge pressure generation with a 45 $\mu m$ chamfer, balanced gear @ 150 bar, 1000 rpm. . . . .	48
4.49	Tilt of bearing without chamfer, balanced gear @ 150 bar, 1000 rpm. . . . .	48
4.50	Tilt of bearing with a 45 $\mu m$ chamfer, balanced gear @ 150 bar, 1000 rpm. . . . .	48
4.51	Separated physical wedge term showing pressure generation due to tilt @ 150 bar, 1000 rpm. . . . .	48
4.52	Separated physical wedge term showing pressure generation due to chamfer @ 150 bar, 1000 rpm. . . . .	48

# List of Tables

1.1	External gear pumps minimum and maximum operation conditions.[1] . . .	2
3.1	Position of the datum plane points. . . . .	32
3.2	Initial conditions for the squeeze velocities. . . . .	32
3.3	Pump geometrical properties. <i>POA = point of application</i> . . . . .	33
4.1	Difference in pump losses at a given operating condition compared to the case without a chamfer. The case without a chamfer are assumed to be 1.0 and a value below indicates decreased power losses and vice versa. . . . .	46

# Nomenclature

## Latin

$\mathbf{F}$  - forces in axial direction

$\mathbf{n}_i$  - normal vector

$\mathbf{T}$  - torque

$\mathbf{V}_i$  - fluid velocity vector

$d$  - distance between the two gears

$DR_d$  - drain leakages at drive gear

$DR_s$  - drain leakages at slave gear

$F_{axial}$  - axial force

$F_{balance}$  - balancing force

$F_{gap}$  - force generate by the lubricating gap

$F_{reliefgrooves}$  - force generate by the relief grooves

$F_{TSV}$  - force generate by tooth space volume

$F_{x,POA}$  - forces in x-direction at the point of application

$F_{y,POA}$  - forces in y-direction at the point of application

$h_b$  - bottom surface, gears lateral surface

$h_t$  - top surface, bushings lateral surface

$h_{T_0}, h_{T_1}, h_{T_2}$  - specific gap height at the three datum points

$h$  - gap height  $h_t - h_b$

$M_x, M_y$  - moments in x-, and y-direction

$p$  - pressure

$POA$  - point of application

$Q_{leakages}$  - leakages on gears lateral side

$R$  - gear radius

$s_0, s_1$  - face boundary nodes

$u_{gears}$  - velocity of the gears

$u_b$  - bottom surface velocity

$u_t$  - top surface velocity

$v_i, v_j, v_k$  - velocity

$x_i, x_j, x_k$  - position in space

$x_{balance}, y_{balance}$  - point-of-application of calculated balance force in x- and y-direction

$x_r, y_r$  - point-of-application of resultant force in x- and y-direction

$x_{POA}$  - position in x-direction of the point of application

$y_{POA}$  - position in y-direction of the point of application

## Greek

$\mathcal{A}$  - area

$\alpha(s)$  - lower gap height

$\beta(s)$  - upper gap height

$\rho$  - density

$\mu$  - dynamic viscosity

$\delta\mathcal{A}$  - area of a cell

$\mathcal{P}_{loss}$  - power loss

$\tau_{xy}, \tau_{zy}$  - viscous shear



# Preface

In this study the micro level surface features have been implemented on the gears lateral side of an external gear pump, in terms of a chamfer. Two different chamfers are investigated in terms of generated hydrodynamic pressures, leakages and power losses. The effect of the chamfers on the tilt of the bushing has been investigated by running a fully balanced simulation.

The work has been carried out from January 2011 to June 2011 at MAHA Fluid Power Research Center, Purdue University, IN, USA with student Johan Magnusson under supervision of Dr. Andrea Vacca.

# Acknowledgements

I would like to express my sincere gratitude to all people that in one way or another have helped me during the time at MAHA Fluid Power Research Center, Purdue University, IN.

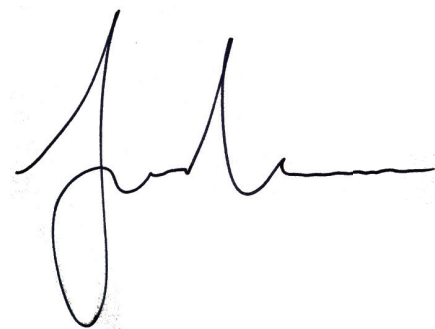
Especially, I would like to thank my supervisor Dr. Andrea Vacca for his continuous support through personal meetings and innovative new perspectives.

The thesis has also benefited from numerous valuable comments and discussions by Ph.D student Sujan Dhar, who also together with the colleagues at MAHA Fluid Power Research Center contributed with a pleasant, enjoyable working atmosphere: Ram Sudarsan, Timothy Opperwall, Davide Cristofori and Wolfgang Schweiger.

Furthermore, thanks MAHA Fluid Power Research Center for providing me the opportunity to perform this work and at the same time having a great time both inside and outside the lab, I enjoyed the time.

Finally, I would like to thank my uncle Per Nilsson who contributed and made my stay in US possible, also my family, who supported me in my work, from the beginning in January until the end of June!

Lafayette, IN June 2011

A handwritten signature in black ink, appearing to read 'Johan Magnusson'. The signature is fluid and cursive, with a large loop at the beginning and a long horizontal tail.

Johan Magnusson





# 1 Introduction

Fluid power are energy transmitted and controlled by pressurized fluid, liquid or gas. Fluid power applications are widely used, commonly in construction machines, agricultural machines, aircrafts and military. The key elements exists as either a pump or a motor and were for several year designed and developed by empirical procedures. Nevertheless, modern design techniques such as FEM (finite element method) have been applied and used for stress analyses, tools to understanding the main flow etc. However, the design procedure is still mainly dependent on empirical studies and there is not yet any advanced design tools to answer many important problems.

The design procedure has made the manufacturers through experience aware of the high level of tolerances and micro level geometry details influence on the system. In literature there is only a few studies that investigates the phenomena of the geometrical micro details. This is due to the complexity of the problem since it involves multiple domains and scales.

This work will prove how it is possible to couple different tools to investigate the problem involving micro level details. Since an existing tool was available for the main flow of external gear machines, it was possible to put an effort of that work, to accomplish the goal of this work, to implement and study the tolerances of the gears lateral profile.

The work itself corresponds to an, un-investigated or not, well known aspect of the external gear machines. One of the secrets in the design of the lateral sides of the gear seems to be this aspect.

This work will study this aspect with the aim of quantifying and proving the impact of different design choices of the operation. A commercial pump will be taken as reference throughout the work.

The work will begin by introducing the reader by showing the functionality of the external gear machine and describing the unit with its details.

## 1.1 External gear pump overview

This introductory chapter are written to help the reader through the report to understand the basics of an external gear pump.

The external gear pump belongs to the hydraulic class of machines named hydrostatic pumps. The hydrostatic pump class has numerous amount of different designs but what makes them as a class is their principle of working by displacement, thereby displacement machines. Furthermore two different groups of the displacement machines exist, they can be categorized by how the motion of the displacement are transferred within the machine. Either by translatory motion, in other words by a piston, or by rotary motion. The rotary motion are performed by vanes, screws or teeth.

If the displacement machine are driven by an external power source is it categorized as a pump and if the motion of the fluid drives the gears it is categorized as motor. Theoretically, the design of pumps and motors is the same but in practice are they designed as either a pump or a motor, this to get an optimal design.

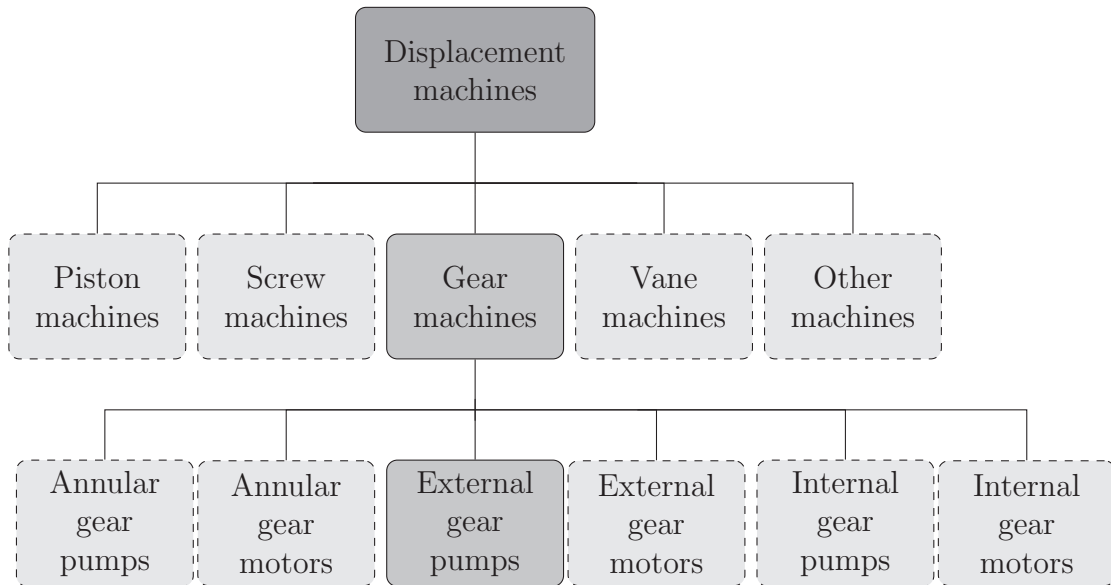


**Figure 1.1** – Classification of displacement machines.[1]

The external gear pumps are basically a housing containing two equal gearwheels, each of them held in a housing. This mechanical simplicity is one big reason for their success, in addition to this the external gear pump is very light, small when it comes to volume, suited for hard conditions and can handle a wide range of different flow rates. At last, the external gear pump is one of the cheapest displacement machines on the market, which makes it a good competitor compared to other displacement machines.

Operation conditions		
	Min	Max
Displacement [ $cm^3/rev$ ]	0.1	50 to 300
Speed [ $rpm$ ]	300 to 700	2000 to 8000
Pressure [ $bar$ ]	80 to 350	400

**Table 1.1** – External gear pumps minimum and maximum operation conditions.[1]

According to Table 1.1 it can be seen that the external gear pump has a big range when it comes to displacements, pressure and speed but the has also a couple of drawbacks. They have fixed displacement volumes, becomes noisy and have a high flow pulsation. To reach favorable efficiencies the production cost will be influenced due to different materials, treatments and higher tolerances.

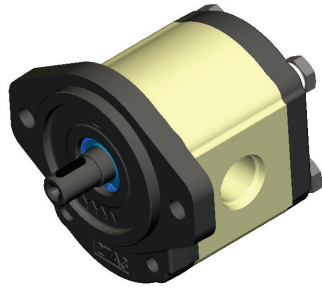


**Figure 1.2** – External gear pump, CASAPPA PLP20 11.2 Standard

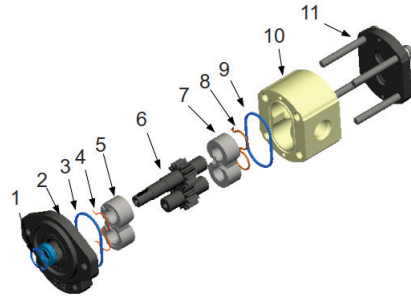


**Figure 1.3** – Exploded view of an external gear pump, CASAPPA PLP20 11.2 Standard.

Figure 1.3 shows an exploded view of an external gear pump. From left to right it contains a sealing to prevent oil leakage (1), the sealing is mounted on the flange (2) followed by the case sealing (3). This is followed by an anti-extrusion ring (4) and a seal which has the same shape as the seal in the following bushing (5), the anti-extrusion ring separates the suction area from the delivery area, this to avoid extrusion of the sealing parts. In general, the bushings are affecting the performance of the machine, internal pressure peaks, cavitation and sealing of the volumes[3].

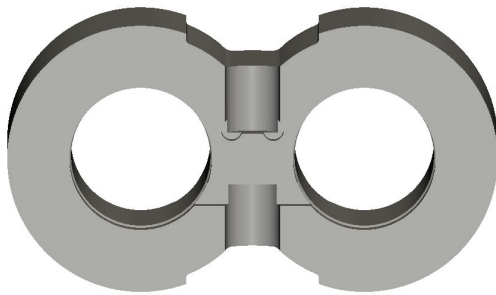


**Figure 1.4** – Front view of the bushing, high pressure port at the top and low pressure port at the lower part. Low pressure connected to the drain.

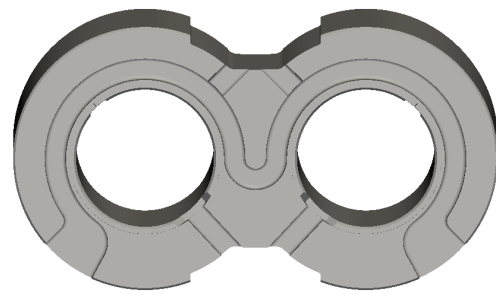


**Figure 1.5** – Back side of the bushing, high pressure port connected to the back side to generate a balancing force. Low pressure port connected to the drain at the lower part.

The external gear pump contains two sliding bushings (or bearing blocks) (5) and (7), one at each side of the two gears (6). The sliding bearings have multiple purposes, they seal the fluid during the transfer process and also works as a communicator between the tooth space volumes, pressure and suction ports, this helps to avoid huge pressure peaks. The communication between the suction and pressure side of the pump are done by creating interstices on the bushing, Figure 1.4 and Figure 1.5. Usually the bushing also play an important role when it comes to the balancing of the pump. Old pumps used perfectly smooth lateral faces and stator where modern pumps are self-balanced. Between the two bushings are the two gears located (6), the driving gears which is connected to an external power source, and the slave gear which is driven by the drive gear.

Above the second bushing, the second anti-extrusion ring (8) and a seal is found, followed by case sealing (9) and the cover (11). At last, the housing (10) which surrounds all parts and contains the suction port (inlet port) and the pressure port (outlet port). Usually the pressure port is larger than the suction port, and the most common way is to

mount them opposite to each other.

When the pump is operating the delivery pressure should be at maximum over the whole upper chamber and the lowest pressure inside the pump will be found at the suction side. The pressure should increase proportionally from the first tooth space volume until it reaches a maximum at the delivery section. This pressure increase causes the pump to feel radial loads which increasing from the suction side to the delivery side. The stresses due to the pressure differences are therefore highest at the delivery area of the pump.

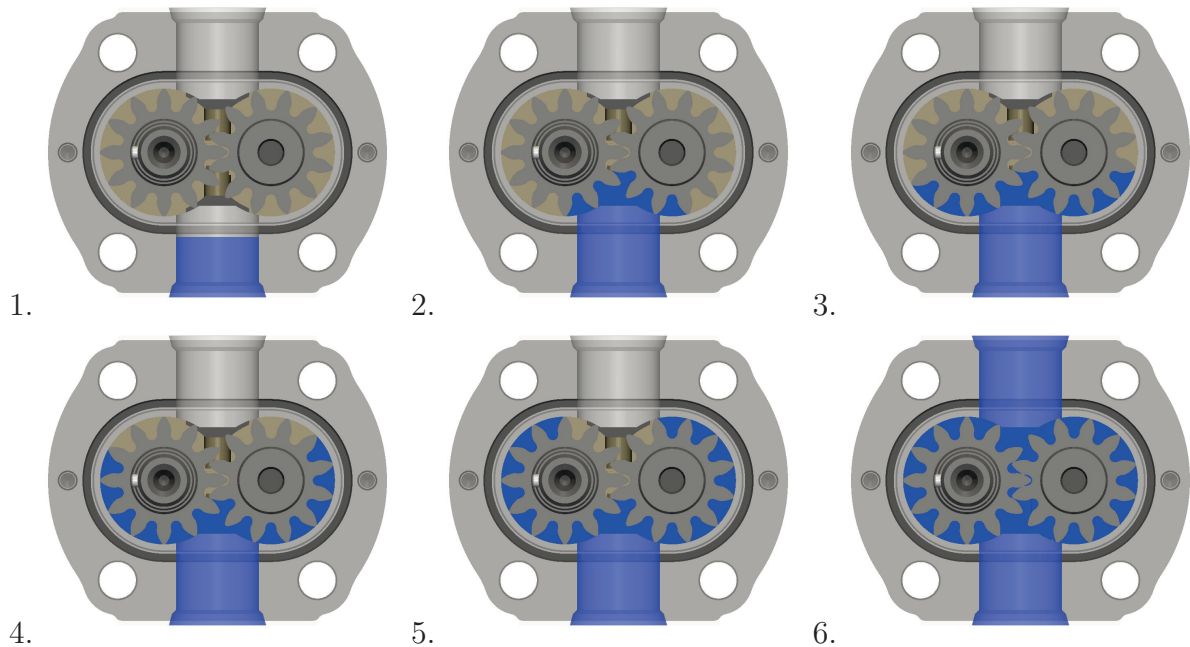


**Figure 1.6** – Meshing process through an external gear pump, basic principles.

The fluid through the pump is transferred by the meshing process which is caused by the sliding elements, i.e rotation of gears inside the pump. The process is well described by Figure 1.6. The process begins with the fluid that enters the gear pump at the low pressure region in the bottom, the gear teeth pushed the fluid around by rotation. These gears creates an expanding volume on the suction side of the pump. The liquid that flows in the cavity will be trapped by the gears as they rotate. The liquid will continuously, travel around the interior of the casing, trapped in the volume created by the gear teeth and the casing. Thereby is the flow rate through the pump depended on the sum of volumes between the gear teeth and casing. An optimal design is therefore, according to a specific gear diameter, to choose as large number of teeth as possible[1]. The fluid transport process ends when the meshing of the gears forces the liquid through the outlet under high pressure, this area is commonly called the discharge chamber[4].

## 1.2 Background and state-of-the-art

Despite the fact, the gear pump is a mechanically simple machine, the limited number of internal elements shows a tendency to influence each other in such way that they strongly complicates the design of the machine. An excellent understanding of the machine is therefore of significant importance when it comes to the design process. This includes understanding of the energy transfer, motion transmission, displacing action, sealing and timing for the lateral elements etc.[2],[5].

These features have been of interest to scientists for years and several analytical and geometrical approaches have been developed. A quite common approach in the literature

is to describe a model for the fluctuations of the external ports. Most common are the lumped parameter models, like [6] and [7] but recently several includes more complex CFD modelling approaches, [8] and [9]. The difference between the two approaches is that the CFD approach contains more complex features and allows a deeper understanding of the problem, like describing the lubricating gap. In these cases is it common to describe the gap with a constant gap height, even if its a big simplification of the problem it still increases the understanding of the gap phenomena.

The phenomena that there occurs a gap between the bearing blocks and the lateral side of the gears are well known, more described in Figure 1.7 and Figure 1.8. This gap occurs in magnitude of microns and are changing according to rotational speed and pressure of the gear pump. According to experimental data, an equilibrium can be reached, which is defined as the position where a balance is reached between the torques and forces acting on the bushings. This is experimentally proved by installing displacement transducers on the end faces of the gear teeth, [10], [11]. In the end is the design of the influenced parts (gears, bushings) attempting to minimize the leakages across the lateral side of the gears even if an adequate fluid film has to exist to prevent wear and increased shear stresses and last also to reduce the noise generation.

The balance is simply achieved by feeding high pressure oil from the high pressure side to the back side of the bushings, this creates a force that should even out the forces generated by the gap itself and the teeth space volumes, Figure 1.4 and Figure 1.5.

MAHA Fluid Power Research Center in Lafayette, IN, are under Dr. Andrea Vacca developing an open-source numerical application in OpenFOAM environment that should be able to predict the lubricating gap inside the external gear pump and by that be able to predict the tilt of the bushings by studying the generated forces. The development of the numerical solver was initially started by Marco Zecchi in the end of 2009, the continuous development was taken into possession by Sujan Dhar which at this date has the responsibility for the developing process, both worked/s under supervision of Dr. Andrea Vacca.

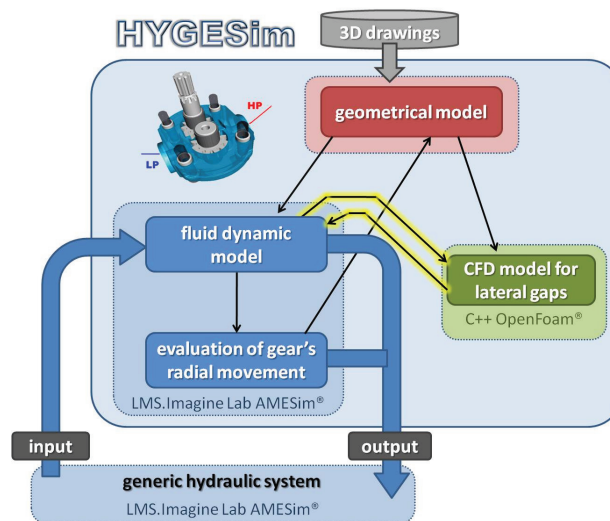


**Figure 1.9** – Structure of the combined HYGESim model with presented flux between the different modules.

The solver for the lubricating gap is more or less a part of a complex fluid dynamic model developed to characterize the flow throughout the entire external gear pump, HYGESim (Hydraulic Gear machines Simulator)[2]. HYGESim was combined with the solver of the lubricating gap to gain a better understanding of the fluid flow field inside the

external gear pump. They are coupled together by exchanging teeth space pressure and leakages. HYGESim solves the internal flow and calculates the pressure inside each tooth space volume at all instantaneous positions during a revolution, the calculated pressure acts as input data, boundary conditions, to the gap solver developed in OpenFOAM. The gap solver calculates the leakages in the gap which are used by the fluid solver HYGESim. The HYGESim modules are showed in Figure 1.9 and describes the flux of data between them.

The numerical gap solver could at the date when the thesis was written, solve the Reynolds equation and give an initial solution to the pressure distribution and the generative forces inside the gap. It was also possible to give a first preview of the actual tilt of the bushing but in the end, to increase the accuracy of the solver and the physical agreement to experimental data and predictions, further implementations has to be made, which brings the background to the purpose of this thesis.

### 1.3 Purpose

According to previous work, there are no investigations performed regarding the micro level surface features. This study is therefore based on the empirical knowledge that tiny geometrical changes can make a significant difference to the system.

It is a well known fact that different manufactures tends to add through the machinery process a chamfer on the gears lateral side in the external gear pump. The shape and size of the chamfer are usually kept in secret by the company itself and even if the effects from the chamfer is positive the physical explanations are unknown. Recent studies, such as [2], [8] and [9] used a simplified approach where the gear profile are assumed flat but to get an advanced understanding of the physical phenomenas that originates from the assumption that micro level surface features can play a significant role, the chamfer implementation to the solver is a natural step in the development.

The micro level surface features should be easy to implement and to modify, it is by that restriction natural to use the CAD drawings as a reference. The development should therefore origin from the CAD drawings and end with an implementation in the numerical gap solver. Continuously the effects generated by the micro level surface features should be investigated and compared to a case without any features in terms of pressure distributions, leakage and shear stress comparisons.

The goal is in short terms to investigate the physical effects generated due to a non-flat gear profile incorporated generally in the machinery process.

### 1.4 Sustainable development

By taking into account the environmental factors a deeper understanding of the generated physical effects is of great importance to be able to continue the development of external gear pumps. The ambition is to decrease the losses in terms of leakages, power and noise. Therefore it is of great importance to continue the theoretical and physical understanding of the external gear pumps when looking in a sustainable development perspective.

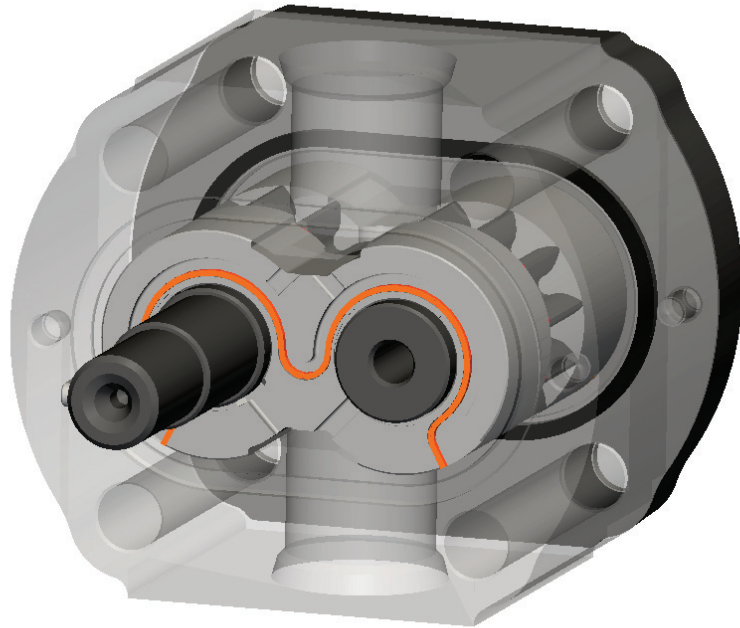


**Figure 1.7** – Transparent view of an external gear pump.

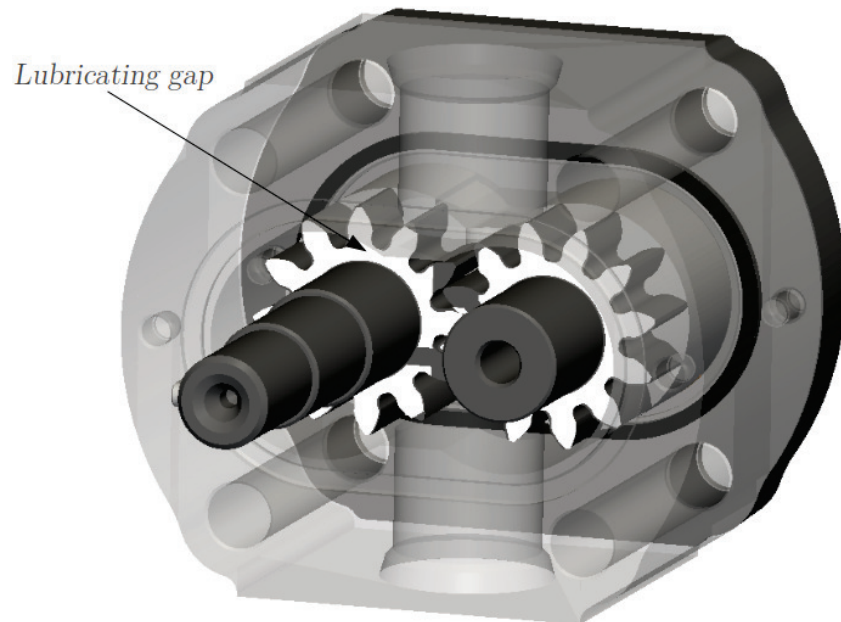


**Figure 1.8** – Transparent view of an external gear pump describing location of the lubrication gap, between the gears and the bushing.

## 2 Theoretical complementary

The derivations and explanations mentioned under the theoretical complementary are written to help the reader with the mathematical understanding of the solved equations and procedures to predict leakages, shear stresses and power losses.

### 2.1 Reynolds Equation

Reynolds equation are mainly derived from Navier-Stokes and the continuity equation, [12]. Reynolds equation takes in consideration the viscosity variations in the film and slip at the bearing surfaces and are generally used to solve lubricated flow problems. Lubricated systems consist of moving surfaces (one may be considered stationary), loaded or unloaded with a thin film between them. The thin film supports the load by the surfaces and minimizes the friction[13]. The derivation of Reynolds equation begins with Navier-Stokes equation with a couple of assumption.

#### 2.1.1 Navier-Stokes equations

$$\frac{\partial \rho v_i}{\partial t} + \frac{\partial \rho v_i v_j}{\partial x_j} = \frac{\partial p}{\partial x_i} + \frac{\partial}{\partial x_j} \left( \mu \frac{\partial v_i}{\partial x_j} \right) \quad (2.1)$$

General assumption:

- By assuming steady-state,  $\frac{\partial \rho v_j}{\partial t}$  will be zero.
- In Reynolds equation the inertial forces are negligible compared to the viscous ones, thereby could  $\frac{\partial \rho v_i v_j}{\partial x_j}$  neglected.
- Gradients in gap direction are much larger than the ones in other directions,  $\frac{\partial v_1}{\partial x_3} \gg \frac{\partial v_3}{\partial x_1}, \frac{\partial v_2}{\partial x_3} \gg \frac{\partial v_3}{\partial x_2}$  and  $v_1 \gg v_3, v_2 \gg v_3$ .
- Pressure is not a function of the gap height,  $p = p(x_1, x_2)$ .

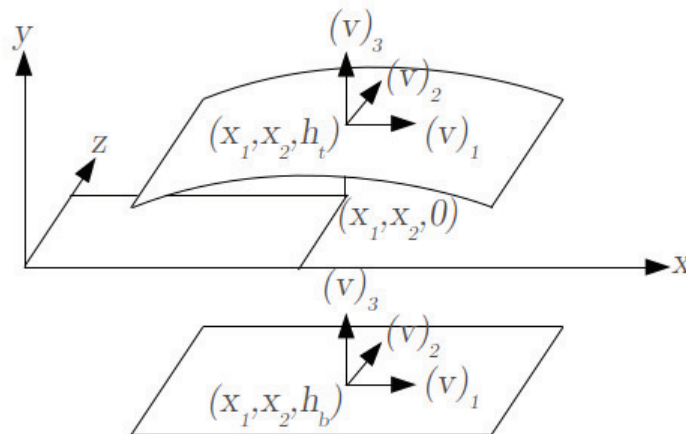


**Figure 2.1** – Coordinate system over a lubrication gap, where h is the gap height.



By this the Navier-Stokes equation can be reduced to

$$\frac{\partial p}{\partial x_i} = \frac{\partial}{\partial x_j} \left( \mu \frac{\partial v_i}{\partial x_j} \right) \quad (2.2)$$

and since  $\frac{\partial v_1}{\partial x_3} \gg \frac{\partial v_3}{\partial x_1}, \frac{\partial v_2}{\partial x_3} \gg \frac{\partial v_3}{\partial x_2}$  the set of equations can be reduced to the following

$$\begin{aligned} \frac{\partial p}{\partial x_1} &= \frac{\partial}{\partial x_3} \left( \mu \frac{\partial v_1}{\partial x_3} \right) \\ \frac{\partial p}{\partial x_2} &= \frac{\partial}{\partial x_3} \left( \mu \frac{\partial v_2}{\partial x_3} \right) \end{aligned} \quad (2.3)$$

Follow by integrating Equation 2.3 twice gives Equation 2.4. Notice that the viscosity is treated as the average value across the film even though it is well known that the viscosity may change across the film due to temperature changes[14].

$$\begin{aligned} v_1 &= \frac{x_3^2}{2\mu} \frac{\partial p}{\partial x_1} + A \frac{x_3}{\mu} + B \\ v_2 &= \frac{x_3^2}{2\mu} \frac{\partial p}{\partial x_2} + C \frac{x_3}{\mu} + D \end{aligned} \quad (2.4)$$

The constants can be determined by imposing the following boundary conditions

$$v_1 = u_t \text{ and } v_2 = v_t \text{ and } x_3 = h_t$$

$$v_1 = u_b \text{ and } v_2 = v_b \text{ and } x_3 = h_b$$

Inserting boundary conditions in Equation 2.4 gives

$$\begin{aligned} u_t &= \frac{h_t^2}{2\mu} \frac{\partial p}{\partial x} + A \frac{h_t}{\mu} + B \\ v_t &= \frac{h_t^2}{2\mu} \frac{\partial p}{\partial y} + A \frac{h_t}{\mu} + B \\ u_b &= \frac{h_b^2}{2\mu} \frac{\partial p}{\partial x} + C \frac{h_b}{\mu} + D \\ v_b &= \frac{h_b^2}{2\mu} \frac{\partial p}{\partial y} + C \frac{h_b}{\mu} + D \end{aligned} \quad (2.5)$$

which after some manipulation gives Equation 2.6. This equation corresponds to the velocity components in the lubricating gap. The derivatives of the velocity components will simply give the velocity gradients.

$$\begin{aligned} v_1 &= \frac{1}{2\mu} \frac{\partial p}{\partial x_1} (x_3^2 - x_3(h_t + h_b) + h_t h_b) + x_3 \frac{u_t - u_b}{h_t - h_b} + \frac{u_b h_t - u_t h_b}{h_t - h_b} \\ v_2 &= \frac{1}{2\mu} \frac{\partial p}{\partial x_2} (x_3^2 - x_3(h_t + h_b) + h_t h_b) + x_3 \frac{v_t - v_b}{h_t - h_b} + \frac{v_b h_t - v_t h_b}{h_t - h_b} \end{aligned} \quad (2.6)$$

Equation 2.6 consists of two components, one due to pressure gradients and one due to dragging effects caused by the walls[12].

### 2.1.2 Continuity equation

Use the continuity equation and integrate with respect to the gap height limits  $h_b$  and  $h_t$ .

$$\frac{\partial \rho}{\partial t} + \frac{\partial(\rho v_i)}{\partial x_i} = 0 \quad (2.7)$$

According to previous assumptions of steady-state flow and incompressible fluid, Equation 2.7 can be reduced to

$$\frac{\partial(v_i)}{\partial x_i} = 0 \quad (2.8)$$

Since the gradients in gap direction are much bigger than the ones in flow direction the solution to the integral can be expressed as

$$\int_{h_b}^{h_t} \frac{\partial v_1}{\partial x_1} dx_3 + \int_{h_b}^{h_t} \frac{\partial v_2}{\partial x_2} dx_3 + \int_{h_b}^{h_t} \frac{\partial v_3}{\partial x_3} dx_3 = 0 \quad (2.9)$$

The intergration in  $x_3$ -direction can be performed directly

$$\int_{h_b}^{h_t} \frac{\partial v_3}{\partial x_3} dx_3 = \int_{h_b}^{h_t} \frac{dv_3}{dx_3} dx_3 = v_3 \Big|_{h_b}^{h_t} = v_{h_t} - v_{h_b} \quad (2.10)$$

With respect to Fig 2.1, assuming the bottom surface below the reference plane, Equation 2.9 can be separated into upper and lover part. This combined with implementing the direct integration in Equation 2.10 gives

$$\int_0^{h_t} \frac{\partial v_1}{\partial x_1} dx_3 + \int_{h_b}^0 \frac{\partial v_1}{\partial x_1} dx_3 + \int_0^{h_t} \frac{\partial v_2}{\partial x_2} dx_3 + \int_{h_b}^0 \frac{\partial v_2}{\partial x_2} dx_3 + v_{h_t} - v_{h_b} = 0 \quad (2.11)$$

$$\int_0^{h_t} \frac{\partial v_1}{\partial x_1} dx_3 - \left( \int_0^{h_b} \frac{\partial v_1}{\partial x_1} dx_3 \right) + \int_0^{h_t} \frac{\partial v_2}{\partial x_2} dx_3 - \left( \int_0^{h_b} \frac{\partial v_2}{\partial x_2} dx_3 \right) + v_{h_t} - v_{h_b} = 0 \quad (2.12)$$

Since  $v_1$  and  $v_2$  are functions depending on  $f(x_1, x_2, x_3)$  with respect to Equation 2.6, Leibnits rule of integration has to be taken in to account

$$\int_0^h \frac{\partial f(x_1, x_2, x_3)}{\partial x_1} dx_3 = -f(x_1, x_2, x_3) \frac{\partial h}{\partial x_1} - \frac{\partial}{\partial x_1} \int_0^h f(x_1, x_2, x_3) dx_3 \quad (2.13)$$

By implementing Leibnits rule on Equation 2.12:

$$\int_0^{h_t} \frac{\partial v_1}{\partial x_1} dx_3 - \left( \int_0^{h_b} \frac{\partial v_1}{\partial x_1} dx_3 \right) + \int_0^{h_t} \frac{\partial v_2}{\partial x_2} dx_3 - \left( \int_0^{h_b} \frac{\partial v_2}{\partial x_2} dx_3 \right) + v_{h_t} - v_{h_b} = 0 \quad (2.14)$$

The following expression is then calculated

$$\begin{aligned}
& -v_1(x_1, x_2, x_3) \Big|_{x_3=h_t} \frac{\partial x_3}{\partial x_1} + \frac{\partial}{\partial x_1} \int_0^{h_t} v_1(x_1, x_2, x_3) dx_3 \\
& - \left( -v_1(x_1, x_2, x_3) \Big|_{x_3=h_b} \frac{\partial x_3}{\partial x_1} + \frac{\partial}{\partial x_1} \int_0^{h_b} v_1(x_1, x_2, x_3) dx_3 \right) \\
& -v_2(x_1, x_2, x_3) \Big|_{x_3=h_t} \frac{\partial x_3}{\partial x_2} + \frac{\partial}{\partial x_2} \int_0^{h_t} v_2(x_1, x_2, x_3) dx_3 \\
& - \left( -v_2(x_1, x_2, x_3) \Big|_{x_3=h_b} \frac{\partial x_3}{\partial x_2} + \frac{\partial}{\partial x_2} \int_0^{h_b} v_2(x_1, x_2, x_3) dx_3 \right) \\
& + v_{h_t} - v_{h_b} = 0
\end{aligned} \tag{2.15}$$

Equation 2.15 can according to the boundary condition be simplified to the following expression

$$\begin{aligned}
& -u_t \frac{\partial h_t}{\partial x_1} - \left( -u_b \frac{\partial h_b}{\partial x_1} \right) + \frac{\partial}{\partial x_1} \int_{h_b}^{h_t} v_1(x_1, x_2, x_3) dx_3 \\
& -v_t \frac{\partial h_t}{\partial x_2} - \left( -v_b \frac{\partial h_b}{\partial x_2} \right) + \frac{\partial}{\partial x_2} \int_{h_b}^{h_t} v_2(x_1, x_2, x_3) dx_3 \\
& + v_{h_t} - v_{h_b} = 0
\end{aligned} \tag{2.16}$$

Continue by substituting from Equation 2.6

$$\begin{aligned}
& -u_t \frac{\partial h_t}{\partial x_1} - \left( -u_b \frac{\partial h_b}{\partial x_1} \right) - v_t \frac{\partial h_t}{\partial x_2} - \left( -v_b \frac{\partial h_b}{\partial x_2} \right) \\
& + \frac{\partial}{\partial x_1} \int_{h_b}^{h_t} \left( \frac{1}{2\mu} \frac{\partial p}{\partial x_1} (x_3^2 + x_3(h_t - h_b) + h_t h_b) + x_3 \frac{u_t - u_b}{h_t - h_b} + \frac{u_b h_t - u_t h_b}{h_t - h_b} \right) dx_3 \\
& + \frac{\partial}{\partial x_2} \int_{h_b}^{h_t} \left( \frac{1}{2\mu} \frac{\partial p}{\partial x_2} (x_3^2 + x_3(h_t - h_b) + h_t h_b) + x_3 \frac{u_t - u_b}{h_t - h_b} + \frac{u_b h_t - u_t h_b}{h_t - h_b} \right) dx_3 \\
& + v_{h_t} - v_{h_b} = 0
\end{aligned} \tag{2.17}$$

Integrate the equation and get the Reynolds equation.

$$\begin{aligned}
& -u_t \frac{\partial h_t}{\partial x_1} - u_t \frac{\partial h_t}{\partial x_2} + u_b \frac{\partial h_b}{\partial x_1} + u_b \frac{\partial h_b}{\partial x_2} \\
& - \frac{\partial}{\partial x_1} \left( \frac{1}{12\mu} \frac{\partial p}{\partial x_1} (h_t - h_b)^3 \right) + \frac{\partial}{\partial x_1} \left( \frac{u_t + u_b}{2} (h_t - h_b) \right) \\
& - \frac{\partial}{\partial x_2} \left( \frac{1}{12\mu} \frac{\partial p}{\partial x_2} (h_t - h_b)^3 \right) + \frac{\partial}{\partial x_2} \left( \frac{u_t + u_b}{2} (h_t - h_b) \right) \\
& + v_{h_t} - v_{h_b} = 0
\end{aligned} \tag{2.18}$$

The Reynolds equation are usually expressed in the so-called general form, where  $h_t - h_b = h$ , together with a couple of rewritings

$$\begin{aligned}
& \underbrace{-\frac{\partial}{\partial x_1} \left( \frac{1}{12\mu} \frac{\partial p}{\partial x_1} (h)^3 \right) - \frac{\partial}{\partial x_2} \left( \frac{1}{12\mu} \frac{\partial p}{\partial x_2} (h)^3 \right)}_I \\
& \underbrace{h \frac{\partial}{\partial x_1} \left( \frac{u_t + u_b}{2} \right) + h \frac{\partial}{\partial x_2} \left( \frac{u_t + u_b}{2} \right)}_{II} + \underbrace{\frac{(u_t + u_b)}{2} \frac{\partial h}{\partial x_1} + \frac{(u_t + u_b)}{2} \frac{\partial h}{\partial x_2}}_{III} \\
& \underbrace{-u_t \frac{\partial h_t}{\partial x_1} - u_t \frac{\partial h_t}{\partial x_2} + u_b \frac{\partial h_b}{\partial x_1} + u_b \frac{\partial h_b}{\partial x_2}}_{IV} + \underbrace{+v_{h_t} - v_{h_b}}_V = 0
\end{aligned} \tag{2.19}$$

Again, notice that no consideration has been taken to varying properties, i.e varying  $\rho$  and  $\mu$ . With this in consideration the ending Reynolds equation will contain a couple of extra terms, for example a local expansion term where the variation of  $\rho$  over time is taken into account.

### 2.1.3 Physical meaning of different terms in Reynolds equation

The meaning of the different terms in the Reynolds equation becomes of importance through out the report. Discussion will be made according to the influence of the different terms to the system. Notice that the term **II.** and **III.** can by using summation rules be converted to one term. This term is not described below and are known as the Couette-term. A more common approach is to describe Reynolds equation as in Equation 2.19. The terms in Equation 2.19 have the following meaning

- I.** Poiseuille term, describes the net flow rates within the lubricated gap due to the pressure gradients.
- II.** Stretch term, consider the rate at which a surface velocity changes in the sliding direction. To develop positive pressure, the surface velocities have to decrease in sliding direction.
- III.** Physical wedge term, is the best known term for pressure generation. It arises from the fact the  $h$  varies across the lubricating gap. The variation of  $h$  causes the flow rate to vary, and a balanced situation can only be reached if balance in the Poiseuille term is imposed. The load carrying capacity of the flow will increase only if the thickness of the lubricant film decreases in flow direction.
- IV.** Translational squeeze term, is the results from the translation of inclined surfaces. For example causes an inclined bearing surfaces translational squeeze.
- V.** Normal squeeze term, provides cushioning effects when the two surfaces in the lubricating gap tends to pressure to each other. It can be told that the Squeeze term and the Physical wedge term are the two main terms generating hydrodynamic force.

## 2.2 Axial balance

To reach a stable solution the summation of the forces acting on the bearing should end up equal to 0. There are totally four different forces assumed to act on the bearing,  $F_{balance}$ ,  $F_{TSV}$ ,  $F_{reliefgrooves}$  and  $F_{gap}$ . It is only the  $F_{balance}$  that pushes the bearing towards the

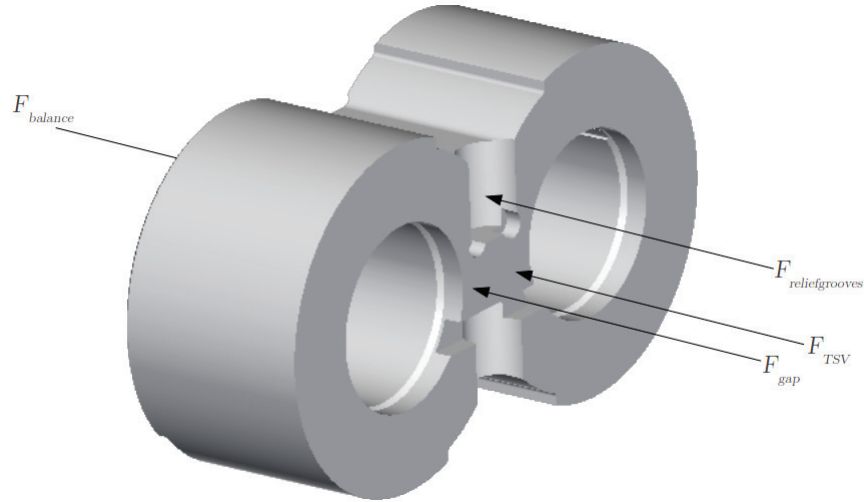


**Figure 2.2** – The bearing with the different forces and their direction against the bushing.

gears, the other forces pushes the bearing away from the gear, Figure 2.2. The balance forces are generated mainly by high pressurized fluid is pushed through tiny accurately measured openings between the output and the bushings[15], Figure 1.4 and Figure 1.5. The high pressurized fluid generates a force that should be equal to axial forces generated by the gears motion. The gear becomes due to this more or less self-balanced and that intends to ensure a good performance over a wide range of pressures.

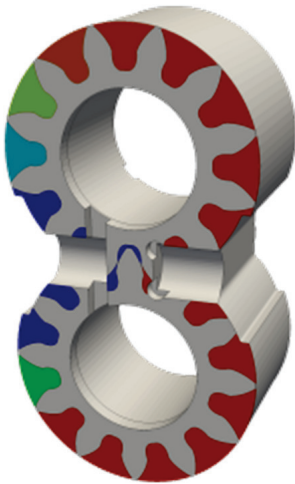


**Figure 2.3** –  $F_{TSV}$

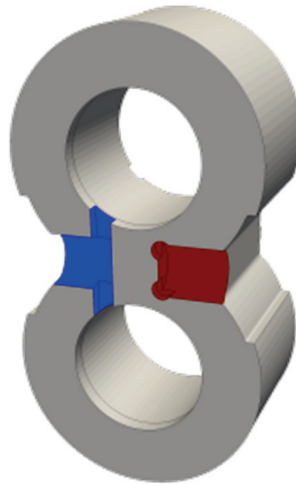


**Figure 2.4** –  $F_{reliefgrooves}$

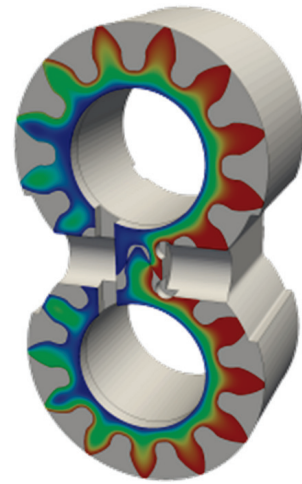


**Figure 2.5** –  $F_{gap}$

The relief groove force ( $F_{reliefgrooves}$ ) are generated by the pressures in the relief grooves. The tooth space force, ( $F_{TSV}$ ) are generated by the axial pressure in the tooth space volume. The calculation of the balance force, relief groove force and the tooth space force are all performed by HYGESim fluid dynamic model and are therefore used as input data. It is only the gap force ( $F_{gap}$ ) that is calculated by the OpenFOAM solver by solving Reynolds equation. The generated force are calculated by a summation over the pressure in each cell multiplied by the area of the cell.

$$F_{gap} = \sum_{i=0}^N p_i \delta \mathcal{A}_i \quad (2.20)$$

By summing up the forces, the result should end up zero, Equation 2.21.

$$\sum \mathbf{F}_z = F_{balance} - F_{reliefgrooves} - F_{TSV} - F_{gap} \equiv 0 \quad (2.21)$$

The point of application of the forces are often of interest to gain a better understanding of the balancing procedure. The point of application are calculated by the OpenFOAM solver by simply summarizing over each one of the cells on pressure field

$$\begin{aligned} F_{x,POA} &= \sum_{i=0}^N p_i x_i \delta \mathcal{A}_i \\ F_{y,POA} &= \sum_{i=0}^N p_i y_i \delta \mathcal{A}_i \end{aligned} \quad (2.22)$$

and then dividing by the generated force

$$\begin{aligned} x_{POA} &= \frac{F_{x,POA}}{\sum_{i=0}^N p_i \delta \mathcal{A}_i} \\ y_{POA} &= \frac{F_{y,POA}}{\sum_{i=0}^N p_i \delta \mathcal{A}_i} \end{aligned} \quad (2.23)$$

## 2.3 Gap height calculation

The variation in gap height is calculated by considering three datum points on the bearings. The bearing are assumed not to bend or deform, the variations are assumed to follow a plane. The three datum points are sketched in Figure 2.6. By using the three points the gap height the plane could be calculated by:

$$h(x, y) = x \frac{2h_{T_2} - h_{T_1} - h_{T_0}}{2(d + R)} + y \frac{h_{T_1} - h_{T_0}}{2R} + \frac{h_{T_0} + h_{T_1}}{2} \quad (2.24)$$

By taking the time derivatives of the gap, the result will be equal to how the gap height changes over time,  $\frac{\partial h}{\partial t}$ .

$$\frac{\partial h}{\partial t}(x, y) = x \frac{2 \frac{\partial h_{T_2}}{\partial t} - \frac{\partial h_{T_1}}{\partial t} - \frac{\partial h_{T_0}}{\partial t}}{2(d + R)} + y \frac{\frac{\partial h_{T_1}}{\partial t} - \frac{\partial h_{T_0}}{\partial t}}{2R} + \frac{\frac{\partial h_{T_0}}{\partial t} + \frac{\partial h_{T_1}}{\partial t}}{2} \quad (2.25)$$

The values on the  $\frac{\partial h}{\partial t}$  are the same as the normal squeeze term in Equation 2.19. The transformation from  $v_{h_t} - v_{h_b}$  are described by simplifications in Section 3.3.1. Another expression for the change in gap height over time are the squeeze velocities, i.e  $\frac{\partial h_0}{\partial t}$ ,  $\frac{\partial h_1}{\partial t}$  and  $\frac{\partial h_2}{\partial t}$ . The sliding velocities are assumed to be unknown from the equilibrium of forces acting on the sliding elements[5], 2.21.

## 2.4 Lateral leakages derivation

Two main leakages occurs inside the external gear pump, radial leakages and lateral leakages. The radial leakages are caused by mainly the casing profile, as result from the break-in process and the position of the bearing. The lateral leakages are caused due to the lubricating gap and are therefore of interest in this thesis.

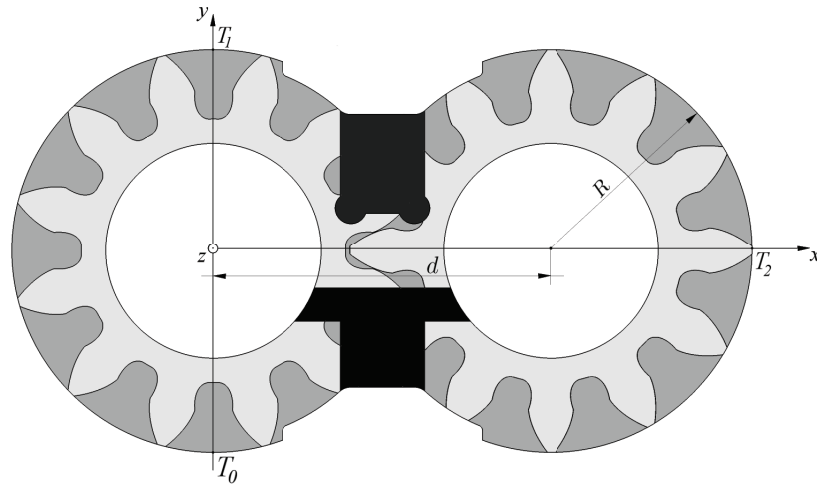


**Figure 2.6** – Sketch over the three datum point at the bearings. Notice the high pressure and low pressure grooves.

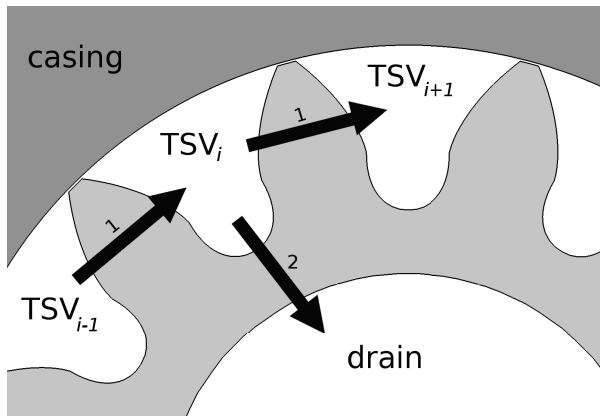


**Figure 2.7** – Leakages between the tooth space volume and leakages to the drain at the gears lateral side.

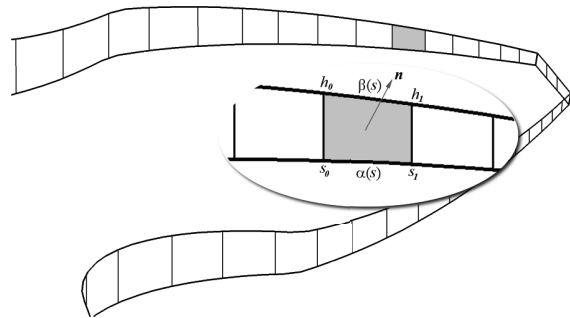


**Figure 2.8** – Boundary patches where the lateral leakages are calculated, including a zoom of a representing boundary face.

The lateral leakages due to the lubricating gap are almost proportional to the gap width, the larger gap, the larger leakages, which in the end increases the flow to the drain or between the teeth space volumes, Figure 2.7. The leakages are calculated with respect to the pressure field of the flow and the velocity contribution. The flow can be evaluated by summation of the integral of fluid velocity over each face of the boundary, Figure 2.8.

$$Q_{leakages} = \sum \iint_{\mathcal{A}} \mathbf{V}_i \mathbf{n}_i \delta \mathcal{A}_i \quad (2.26)$$

As seen in Figure 2.8,  $\mathbf{n}$  is the normal vector of the face where the  $\mathbf{V}$  is the fluid velocity. The fluid velocity can be derived by the same procedure as in the Reynolds equation, i.e. assuming similar assumption and boundary conditions, which ends up with Equation 2.6. Additionally, the lateral side of the gears are assumed to be the only part in motion, i.e. the bearing motion is zero, which gives  $u_t = 0$  and  $v_t = 0$ . The statement re-formulates Equation 2.6 to

$$\begin{aligned}
v_1 &= \frac{1}{2\mu} \frac{\partial p}{\partial x_1} (x_3^2 - x_3(h_t + h_b) + h_t h_b) - \frac{x_3 u_b}{h_t - h_b} + \frac{u_b h_t}{h_t - h_b} \\
v_2 &= \frac{1}{2\mu} \frac{\partial p}{\partial x_2} (x_3^2 - x_3(h_t + h_b) + h_t h_b) - \frac{x_3 v_b}{h_t - h_b} + \frac{v_b h_t}{h_t - h_b}
\end{aligned} \tag{2.27}$$

By integration over the boundaries face width and the gap height, described in Figure 2.8, the leakage flow can be calculated by

$$Q_{leakages} = \int_{s_0}^{s_1} ds \int_{\alpha(s)}^{\beta(s)} (un_1 + vn_2) dx_3 = \int_{s_0}^{s_1} ds \int_{h_b}^{h_0 + \frac{h_1 - h_0}{s_1 - s_0} s} (un_1 + vn_2) dx_3 \tag{2.28}$$

where  $h_0 + \frac{h_{t1} - h_{t0}}{s_1 - s_0} s$  takes into account the tilt on the bearing and  $h_t$  has in Equation 2.27 to be replaced by  $h_0 + \frac{h_{t1} - h_{t0}}{s_1 - s_0} s$ . The tilt on the bearing is assumed to be linear, therefore the tilt over the patch elements is also linear. Assuming that  $s_0 = 0$  and  $s_1 = \delta$  and by integrating Equation 2.28 together with some manipulations the leakages over the boundaries containing  $N$  faces can be expressed with the following summation

$$\begin{aligned}
Q_{leakages} &= \sum_i^N \left[ -\frac{\delta_i}{48} \left( \left( n_{1i} \frac{1}{\mu} \frac{\partial p}{\partial x_1} \Big|_i + n_{2i} \frac{1}{\mu} \frac{\partial p}{\partial x_2} \Big|_i \right) \right. \\
&\quad \left. (-4h_b^3 + 6h_{1i}h_b^2 + 6h_{0i}h_b^2 - 4h_{1i}^2h_b - 4h_{0i}^2h_b - 4h_{0i}h_{1i}h_b + h_{0i}^3 + h_{0i}^2h_{1i} + h_{0i}h_{1i}^2 + h_{1i}^3) \right) \\
&\quad \left. + \frac{\delta_i(h_{0i} + h_{1i} - 2h_b)}{4} (un_1 + vn_2) \right] \tag{2.29}
\end{aligned}$$

The leakage formulation takes into account both the tilt on the bearing side of the gap and the surface variations due to a non-uniform chamfer on the gears. Equation 2.29 is also very similar to the equation derived in [5], if  $h_b$  is assumed 0, i.e without a chamfer, the ending equation will be equal to the one in [5].

The leakage equation consists of two parts, the first part takes into account the pressure distribution due to the pressure gradient of the flow, the second part takes into account the velocity contribution, as mentioned before.

## 2.5 Shear stress derivation

The viscous shear stresses can be calculated by first deriving the two equations for the velocity, Equation 2.6 due to  $x_3$ . The derivation of Equation 2.6 ends of with the following result

$$\begin{aligned}
\frac{\partial v_1}{\partial x_3} &= \frac{1}{2\mu} \frac{\partial p}{\partial x_1} (2x_3 - (h_t + h_b)) + \frac{u_t - u_b}{h_t - h_b} \\
\frac{\partial v_2}{\partial x_3} &= \frac{1}{2\mu} \frac{\partial p}{\partial x_2} (2x_3 - (h_t + h_b)) + \frac{u_t - u_b}{h_t - h_b}
\end{aligned} \tag{2.30}$$

The viscous shear acting on the gear or the bushing can be expressed as

$$\begin{aligned}
\tau_{zx} &= \mu \left( \frac{\partial v_3}{\partial x_1} + \frac{\partial v_1}{\partial x_3} \right) \\
\tau_{zy} &= \mu \left( \frac{\partial v_3}{\partial x_2} + \frac{\partial v_2}{\partial x_3} \right)
\end{aligned} \tag{2.31}$$



Same assumptions are made as in Section 2.1, i.e that the gradients in gap direction are much larger than in the other directions,  $\frac{\partial v_i}{\partial x_3} \gg \frac{\partial v_i}{\partial x_1}, \frac{\partial v_i}{\partial x_2} \gg \frac{\partial v_i}{\partial x_2}$ . This reduces the shear stress equation, Equation 2.31 to

$$\begin{aligned}\tau_{zx} &= \mu \frac{\partial v_1}{\partial x_3} = \frac{1}{2} \frac{\partial p}{\partial x_1} (2x_3 - (h_t + h_b)) + \mu \frac{u_t - u_b}{h_t - h_b} \\ \tau_{zy} &= \mu \frac{\partial v_2}{\partial x_3} = \frac{1}{2} \frac{\partial p}{\partial x_2} (2x_3 - (h_t + h_b)) + \mu \frac{u_t - u_b}{h_t - h_b}\end{aligned}\quad (2.32)$$

This allows calculation of the viscous shear stress acting on the gear or at the bushing in the following way

$$(\tau_{zx})_{x_3=h_b} = \left( \mu \frac{\partial v_1}{\partial x_3} \right)_{x_3=h_b} = \frac{1}{2} \frac{\partial p}{\partial x_1} (h_b - h_t) + \mu \frac{u_t - u_b}{h_t - h_b} \quad (2.33)$$

$$-(\tau_{zx})_{x_3=h_t} = - \left( \mu \frac{\partial v_1}{\partial x_3} \right)_{x_3=h_t} = \frac{1}{2} \frac{\partial p}{\partial x_1} (h_b - h_t) - \mu \frac{u_t - u_b}{h_t - h_b} \quad (2.34)$$

$$(\tau_{zy})_{x_3=h_b} = \left( \mu \frac{\partial v_2}{\partial x_3} \right)_{x_3=h_b} = \frac{1}{2} \frac{\partial p}{\partial x_2} (h_b - h_t) + \mu \frac{u_t - u_b}{h_t - h_b} \quad (2.35)$$

$$-(\tau_{zy})_{x_3=h_t} = - \left( \mu \frac{\partial v_2}{\partial x_3} \right)_{x_3=h_t} = \frac{1}{2} \frac{\partial p}{\partial x_2} (h_b - h_t) - \mu \frac{u_t - u_b}{h_t - h_b} \quad (2.36)$$

The derivation is very similar to the one derived in [14], the difference between the derivations is that the present one takes into account micro level surface features, which means that a chamfer could be taken into account. Notice that there are two parts that generates the shear stress, the first part arises from the pressure gradient inside the gap and the second one arises from rotation rotational speed of the gears. In a physical aspect, both and increased pressure and an increased rotational speed will increase the viscous shear stress, i.e the losses of the pump.

## 2.6 Power losses

The viscous shear stress is as mentioned in Section 2.5, losses in the pump. The losses could be measured in terms of energy (J/s) by calculating the torque and multiply it with the rotational speed of the gears. The torque is calculated by

$$\mathbf{T} = \sum_{i=0}^N 2\mathcal{A}_i(\mathbf{r}_i \times \boldsymbol{\tau}_i) \quad (2.37)$$

The reason why Equation 2.37 is multiplied by two is due to the fact the there are two lubricating gaps in an external gear pump, one on each side of the gear. The energy losses in terms of joules per second could easily be calculated by

$$\mathcal{P}_{loss} = \mathbf{T}\omega \quad (2.38)$$

## 3 Modelling approach

This chapter describes the modeling approach used during the project by first introducing the mesh generation and its procedure and benefits. This is followed by a description of

the used boundary conditions and the implementations in OpenFOAM. The theory behind the implementations are found in the Theoretical Complementary, Section 2.

The modelling approaches are performed on a CASAPPA Standard external gear pump[16], Figure 1.2. Shell Tellus Oil T46[17] oil was used as fluid medium during the simulations.

### 3.1 Mesh generation

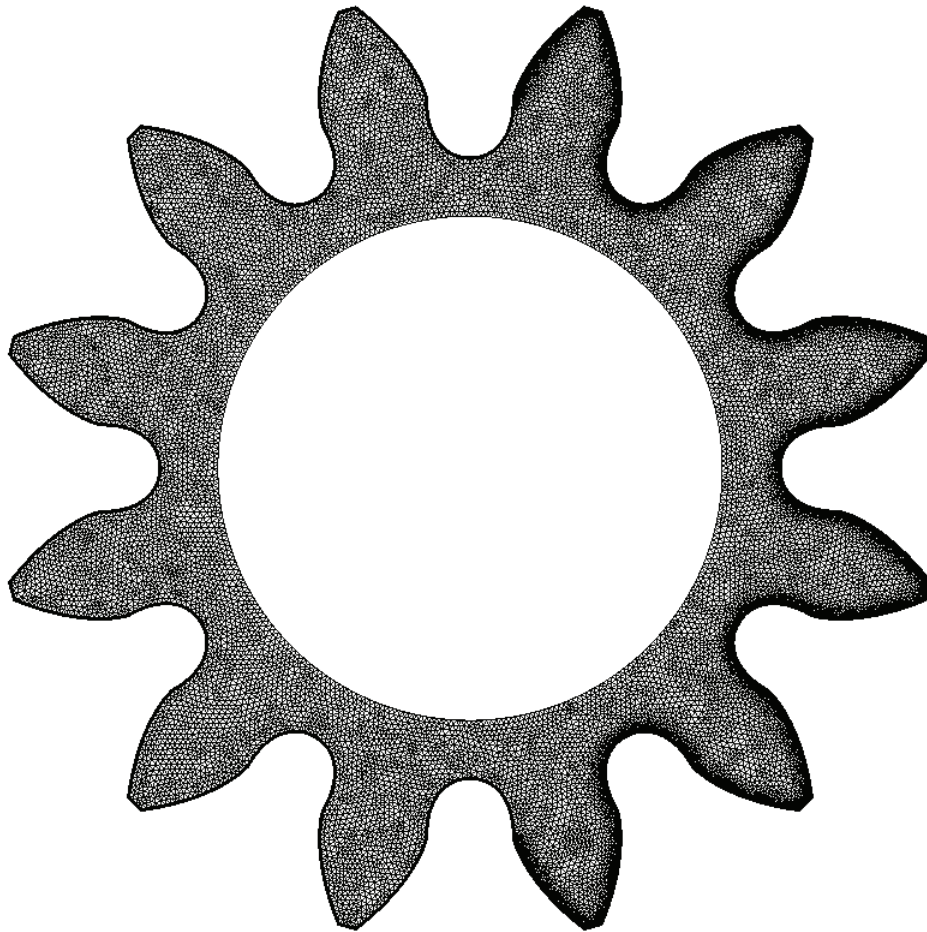
The mesh generation was performed by ANSYS Workbench 12.1 and its meshing software Meshing. The input to ANSYS was one, out of the two gears, taken from the CAD drawings. The gears were exported to a STL-file which later was read by ANSYS. The generated mesh for the drive gear from ANSYS was duplicated, translated and rotated by OpenFOAMs mesh manipulation tools, some in-house built utilities, for example a utility smoothen boundaries and keep track of the patch names.

To be able to fully describe a proper chamfer, boundary layers had to be added to the gears, the size and number of boundary layers were changed according to the size of the chamfer. An amount of 15 to 20 boundary layers were chosen to smoothly represent the chamfer in all cases. Except for the boundary layers, the cell size on the gear was set to  $1e - 4$  m. This has been proven by earlier simulations to give a proper resolution of the mesh and in the end the results. Refinements on the mesh were performed on the right side of the gear on the teeth that neighbor, or will neighbor due to rotation of the gears, to the high pressure and low pressure grooves, Figure 3.1. The refinements were performed to avoid overlapping cells due to the projections of the grooves. It was found out during the project that the smoothing of boundaries at the high and low pressure grooves were very sensitive to thin, small boundary layers. As mentioned earlier, it was only one of the two gears that was extracted from the CAD drawings. The gear contains 12 teeth and because of that the slave gear had to be rotated a half tooth,  $15^\circ$  and translated in x-direction, to match the drive gear. To fully take advantage of the refinements, i.e match the refinements from the drive gear with the slave gear, the slave gear was rotated additionally  $150^\circ$ , see Figure 3.1.

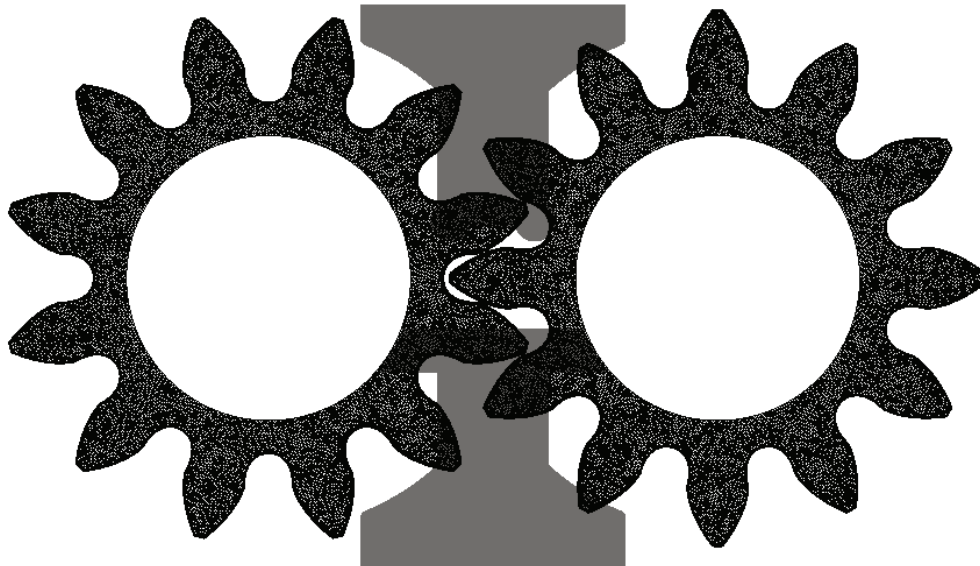
#### 3.1.1 Mesh rotation

To be able to simulate the lubricant gap of an external gear pump a dynamic mesh had to be considered. A dynamic mesh is capable to follow the rotation of the two gears with a high level of accuracy. The raw mesh of the two gears, must be modified during the simulation according to the angular position of the gears.

The grooves at the bearing, the high and low pressure groove, play a significant role on the lubricating gap. Within the grooves, there is no leakage flow and the instantaneous pressure is uniform and equal to the pressure at the suction side (inlet) or pressure side (outlet). Due to this, the regions on the lubricating gap that interact with the groove, do not have to be considered when solving Reynolds equation. By this fact, the cells that occur within the grooves, have to be eliminated, Figure 3.2. The removed cells create a rough surface of cells that has to be smoothen out to preserve the geometrical details of the geometry. The process is simple, cell nodes closest to the boundary are moved to perfectly follow the geometrical details, see Figure 3.3 and Figure 3.4. To simulate the rotation of the gears and to keep the preservation of the geometrical details 30 different meshes were produced, the difference between them are the rotation of the gears, the gears are rotated  $1^\circ$  each step i.e dynamic mesh. The rotation of the gears are symmetric and repetitive after  $30^\circ$ , because of  $360^\circ/12 = 30^\circ$ . So, the projection of the grooves, the smoothening of the

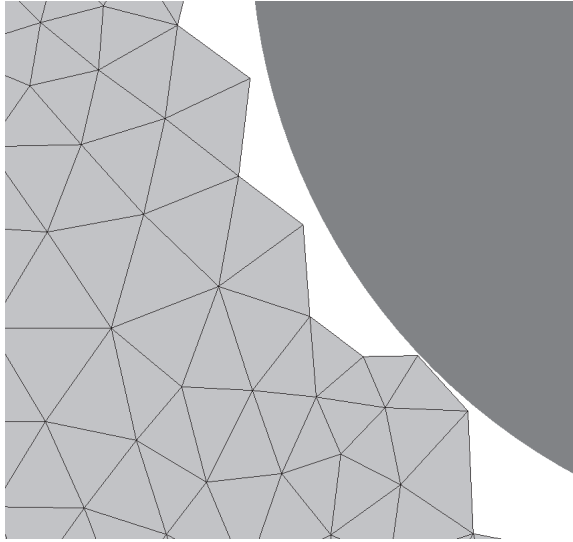


**Figure 3.1** – Mesh with boundary layers and refinements made in ANSYS Workbench.

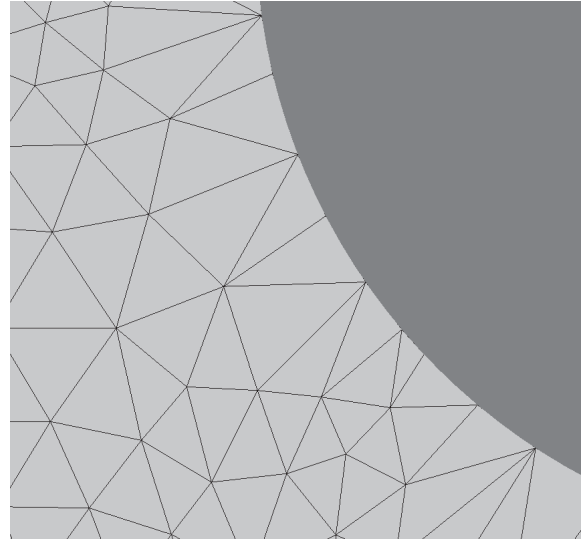


**Figure 3.2** – Mesh with the high pressure and low pressure ports. Cells intersecting with the ports are removed.

boundaries are only being performed 30 times. This approach of using rotation are chosen because it simplifies the solving procedure and is very flexible by excluding all information about the pressure grooves and rotation of the gears. The solver is then focused only

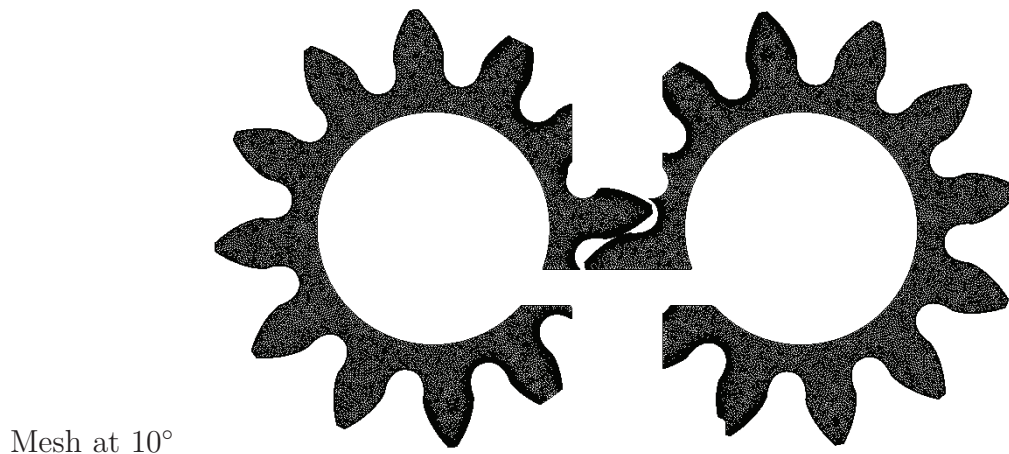
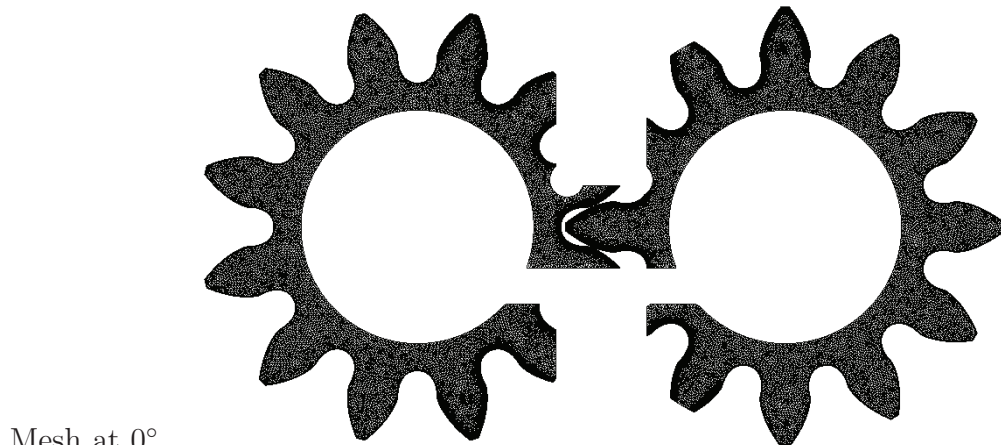


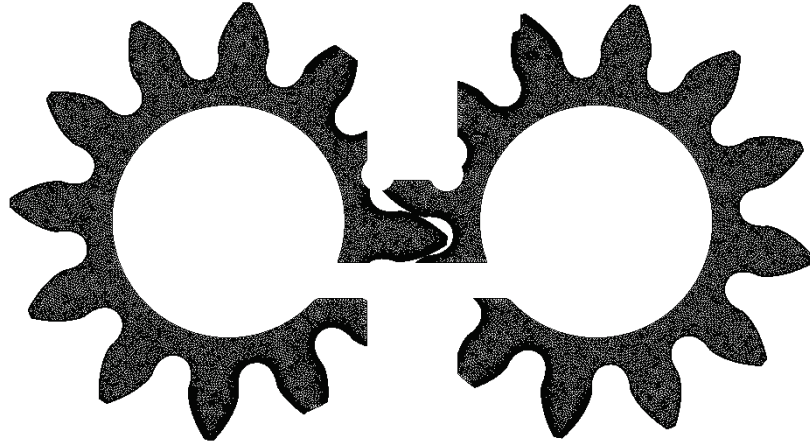
**Figure 3.3** – Non-smooth surface.



**Figure 3.4** – Smooth surface which perfectly follow the geometrical details.

to solve the Reynolds equation without any mesh considerations, just to re-load a new mesh for each time-step. The time-step for the simulations are perfectly matched to  $1^\circ$  of rotation, due to the rotational speed. The final mesh is showed below for three different angles, Figure 3.5.





Mesh at 20°

Figure 3.5 – Mesh with 100  $\mu\text{m}$  chamfer at different angular positions.

### 3.2 Boundary conditions

The pressure boundary conditions are taken from HYGESim (HYdraulic GEAr machines Simulator) fluid dynamic model, Section 1.2. HYGESim is developed to solve the internal flow of an external gear pump and calculate the pressure inside each tooth space volume. The output from HYGESim contains the instantaneous or time varying pressure pressure inside each tooth space volume which are applied to the matching patch on the domain, which is done for each of the angular positions of the mesh. This means that the boundaries has to be reread at each angular position by OpenFOAM since the instantaneous pressure changes due to rotation inside each tooth space volume.

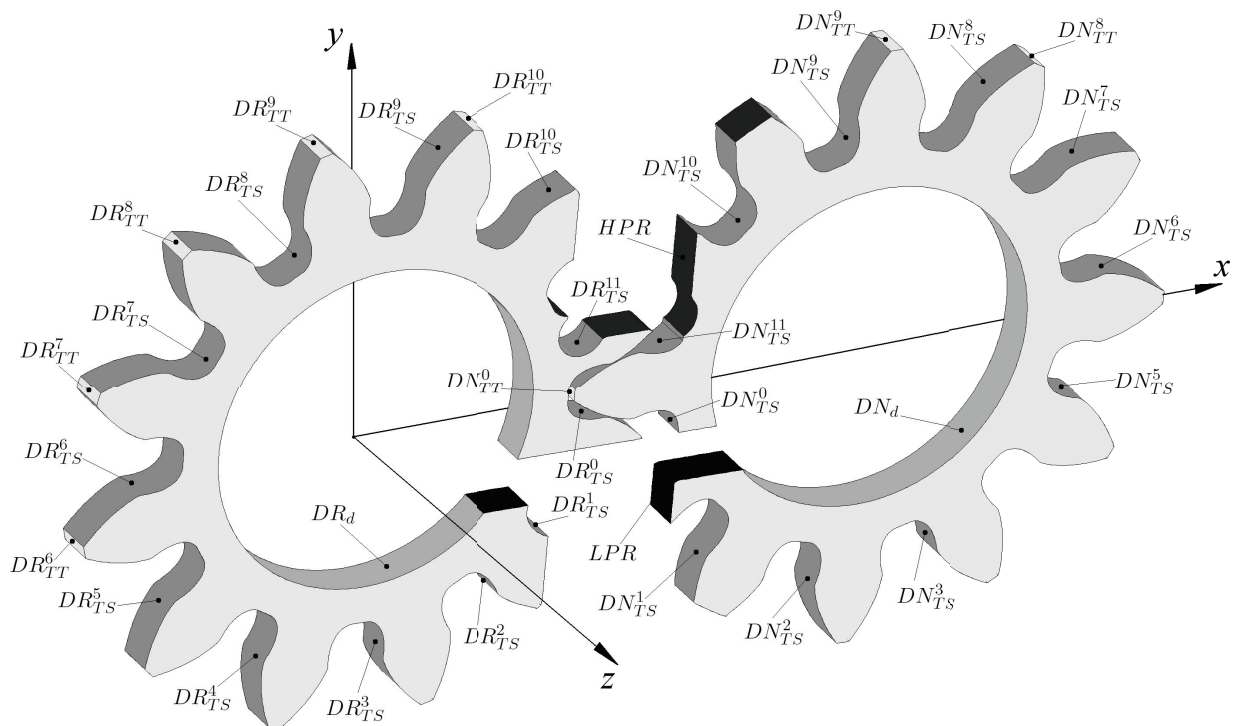


Figure 3.6 – Boundary patches along the drive and slave gear.

An illustrative figure over the boundary patches can be seen in Figure 3.6. All 12 gear teeth are shown in Figure 3.6 where the drive gear patches are labeled  $DR^i_{TS}$  or  $DR^i_{TT}$ , and slave gear  $DN^i_{TS}$  or  $DN^i_{TT}$ , TS refers to tooth space and TT to tooth tip.  $DR_d$  and

$DN_d$  are the gear drains. At last, between the gears, the  $HPR$  and  $LPR$  are found, high pressure port and low pressure port respectively. The pressure is assumed to be uniform and equal to the drain pressure on the gears drain, on the relief grooves, the pressure is, as mentioned earlier equal to the high and low pressure ports. The teeth tips are assumed to have a linearly varying pressure along each boundary, which is based on the hypothesis of laminar flow in the gap between the tooth tip and the casing of the pump.

By fully reread all boundaries between each time-step and move to a new mesh with an updated angular position, complex phenomenas like pressure peaks and cavitation can be taken into account during the simulation.

Two different boundary conditions from HYGESim were used during the project, one HYGESim boundary condition that assumes perfect sealing. This one were used in the simulations when the balancing part of the solver where activated. The reason why the perfect sealing boundary conditions were used originates from the fact the it was found out to be more stable. The other one, the more realistic HYGESim data, are used on every cases where the gap height are fixed.

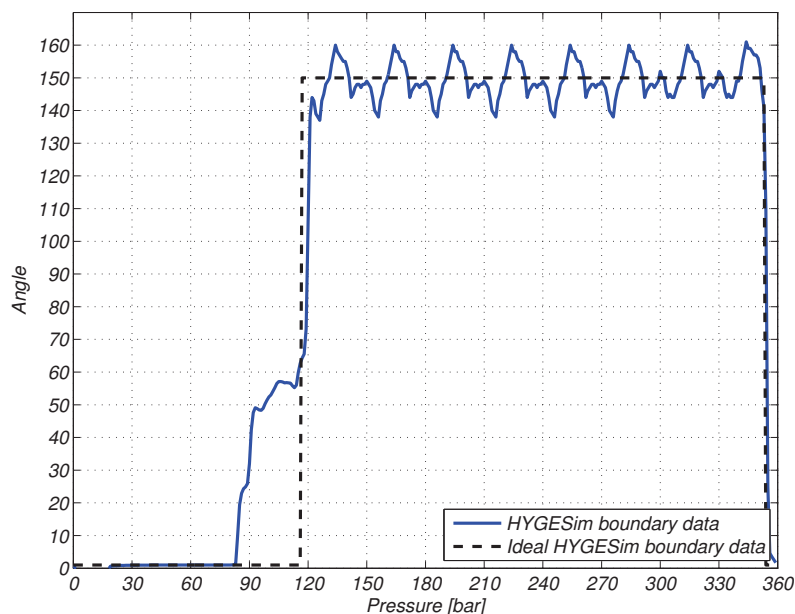


**Figure 3.7** – Difference between the two used boundary conditions from HYGESim.

The difference between the boundaries are plotted in Figure 3.7. The biggest difference between the two boundaries is that the perfect sealing boundary changes pressure instantly at the high pressure groove, and instantly back later. Another difference is that the perfect sealing boundary assumes constant pressure during the meshing process, where the other one does not. Both boundaries turn back to low pressure again as soon as the angular position is equal to the end of the high pressure port, Figure 3.8.

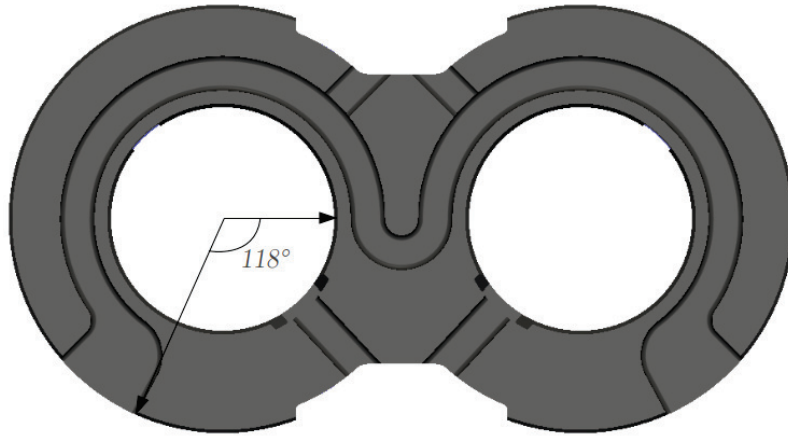


**Figure 3.8** – Back side of the bearing, showing the high pressure groove and its start at  $118^\circ$ .

The instant change for the ideal HYGESim boundary occurs at  $118^\circ$ , the reason for this and for both boundaries are the high speed groove on other side of the bearing, showed in Figure 3.8. The high speed groove prevents an unbalanced bearing by allowing high pressure oil balance the forces acting on the bearing, described in Section 2.2.

### 3.3 OpenFOAM solver and implementations

The simulations in this work were performed by the open-source CFD software OpenFOAM [18], version 1.6.x. The solver for computing is an completely in-house developed by MAHA Fluid Power Research Center[19] and gives a prediction of the lubricating gap by solving Reynolds Equation, Equation 2.19. In addition to this, functions such as separation of the different terms in Reynolds equation, implementation of geometrical changes to the gears lateral profile and leakage calculations are performed by additional implementations to the solver. The solver is under development and more functions are assumed to be implemented in the future.

#### 3.3.1 Solving Reynolds Equation

The derivation of Reynolds equations are found under Section 2.1. The derivation assumes that both top and bottom plates are moving but the simulations in this work allow some simplifications of Equation 2.19:

- The surface in motion is the bottom surface, it is defined by the gears lateral side, i.e the gears and its rotational speed,  $u_b = u_{gears}$ .
- The top surface, the bearing side are fixed,  $u_t = 0$ .
- $v_{h_t} - v_{h_b}$  defines the changes in gap height, the squeeze velocity. The change on the gears lateral side is assumed zero, it is assumed that the bearing side contributes with the change in gap height. The velocity term can be rewritten into time derivative of the gap height,  $\frac{\partial h}{\partial t}$ .

Equation 2.19 are therefore simplified to:

$$\begin{aligned}
 & -\frac{\partial}{\partial x_1} \left( \frac{1}{12\mu} \frac{\partial p}{\partial x_1} (h)^3 \right) - \frac{\partial}{\partial x_2} \left( \frac{1}{12\mu} \frac{\partial p}{\partial x_2} (h)^3 \right) \\
 & + h \frac{\partial}{\partial x_1} \left( \frac{u_{gears}}{2} \right) + h \frac{\partial}{\partial x_2} \left( \frac{u_{gears}}{2} \right) + \frac{u_{gears}}{2} \frac{\partial h}{\partial x_1} + \frac{u_{gears}}{2} \frac{\partial h}{\partial x_2} \\
 & + u_{gears} \frac{\partial h_b}{\partial x_1} + u_{gears} \frac{\partial h_b}{\partial x_2} + \frac{\partial h}{\partial t} = 0
 \end{aligned} \tag{3.1}$$

Equation 3.1 is represented in OpenFOAM by, note that  $h = h_t - h_b$ :

```

lduMatrix::solverPerformance sp = solve
(
    - fvm::laplacian(pow( ((*ht) - (*hb)), 3.0)/(12.0*(mu)), (*p))
    + ((0.50>(*Ugears)) & (fvc::grad((*ht) - (*hb))))
    + ((*Ugears) & (fvc::grad(*hb)))
    + (((*ht)-(*hb)) * (fvc::div(*Ugears)/2))
    + (*dhdt)
);

```

It can be seen that the solver solves the Reynolds equation on a 2D-mesh.  $h_b$ ,  $h_t$ ,  $p$ ,  $u_{gears}$  and  $\frac{\partial h}{\partial t}$  are fields only on the 2D mesh with x and y coordinates but where the value on the field are given in the third direction. This knowledge is very important when it comes to the understanding of the solver.

### 3.3.2 Creation of gears lateral profile

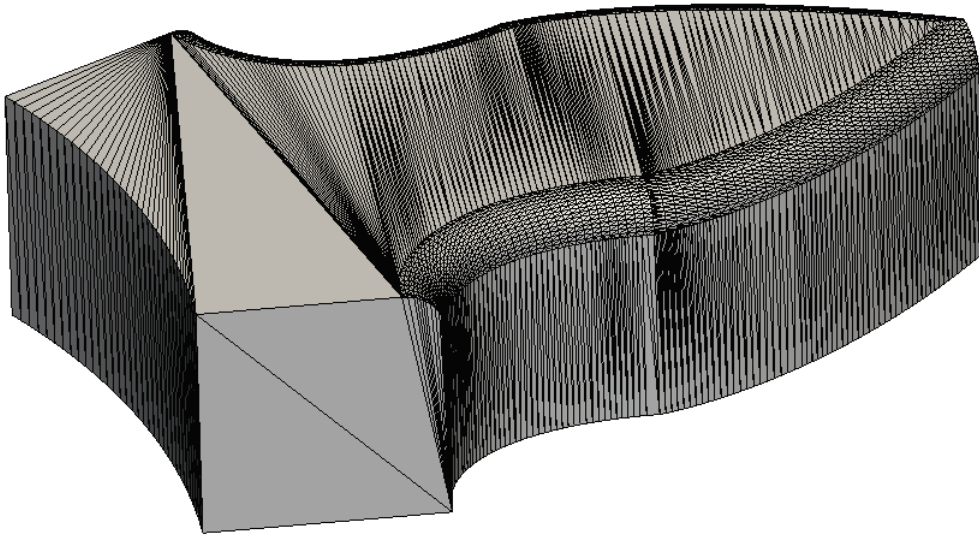
As mentioned earlier the implementation of the micro level surface features should be done with respect to the CAD drawing of the gear pump. This will in the end allow both the user and the pump developer to easily change geometrical shapes of the gear profile. Briefly, the conversation from CAD-drawings to OpenFOAM friendly data was carried out by exporting a single tooth of a complete gear to a .STL-file. The tooth surface has to be converted to become OpenFOAM friendly input data. OpenFOAM loads the data, links the data to a field with a searching algorithm, which then were used in the simulation.



Figure 3.9 – hbFieldMaker

The application used to convert the information from the CAD drawings to OpenFOAM were performed by hbFieldMaker, which was developed during the project by the author in a C++ environment. The application allows refinements of the field by using an implementation of the open-source meshing software gMSH [20] and the only input data that is required to be set-up by the user is the .STL-file from the CAD and the outer radius of the tooth.





**Figure 3.10** – Surface geometry described by a STL file.

The extracted .STL-file contains information about the tooth surface, it describes the tooth by raw unstructured triangles in ASCII format, see Figure 3.10, which is the input to the hbFieldMaker. The hbFieldMaker selects nodes that have a normal in z-direction larger than 0, i.e the upper surface of the tooth including the chamfer. Continuously, hbFieldMaker moves the tooth to a correct position in space according to the user input by an iterative process. The ending part is to duplicate the tooth and rotate it to create a complete gear and finally output the information to a file, which in the end is read by OpenFOAM.

To speed up the searching algorithm in OpenFOAM, the nodes from the complete surface are splitted into 8 parts according to the angular position of the nodes. This was done since it was found out that the searching algorithm in OpenFOAM to link the chamfer to a field was very time consuming. The different parts are represented by different columns in the input file for OpenFOAM, Figure 3.11. The searching algorithm will be explained in more details in Section 3.3.3.

$$\begin{bmatrix}
 x_{i,(0\dots\frac{\pi}{4})} & y_{i,(0\dots\frac{\pi}{4})} & h_{b,i,(0\dots\frac{\pi}{4})} & x_{i,(\frac{\pi}{4}\dots\frac{\pi}{2})} & \cdots & x_{i,(\frac{7\pi}{4}\dots 2\pi)} & y_{i,(\frac{7\pi}{4}\dots 2\pi)} & h_{b,i,(\frac{7\pi}{4}\dots 2\pi)} \\
 x_{i+1,(0\dots\frac{\pi}{4})} & y_{i+1,(0\dots\frac{\pi}{4})} & h_{b,i+1,(0\dots\frac{\pi}{4})} & x_{i+1,(\frac{\pi}{4}\dots\frac{\pi}{2})} & \cdots & x_{i+1,(\frac{7\pi}{4}\dots 2\pi)} & y_{i+1,(\frac{7\pi}{4}\dots 2\pi)} & h_{b,i+1,(\frac{7\pi}{4}\dots 2\pi)} \\
 \vdots & \vdots & \vdots & \vdots & \ddots & \vdots & \vdots & \vdots \\
 x_{m,(0\dots\frac{\pi}{4})} & y_{m,(0\dots\frac{\pi}{4})} & h_{b,m,(0\dots\frac{\pi}{4})} & x_{m,(\frac{\pi}{4}\dots\frac{\pi}{2})} & \cdots & x_{m,(\frac{7\pi}{4}\dots 2\pi)} & y_{m,(\frac{7\pi}{4}\dots 2\pi)} & h_{b,m,(\frac{7\pi}{4}\dots 2\pi)}
 \end{bmatrix}$$

**Figure 3.11** – Input-file to OpenFOAM, the different columns represent different angles on the complete gears lateral profile.  $i$  represents row and  $0\dots\frac{\pi}{4}$  the range of angular position of the nodes.

### 3.3.3 Implementation of micro level surface features in OpenFOAM

The micro level surface features is built up in OpenFOAM as a pre-process before the actual solving of the Reynolds equation begin. Huge matrices had to be used during the building of the gear profile, this was solved by using the open-source GSL's library[21] and

its `gsl_matrix`. Briefly, when the solver was executed by the user, the solver first loaded the `hbField.C` which is the implementation that builds and generates the chamfer profile.

`hbField.C` loads the time derivatives, sets the mesh for the first angular position and reads the output file from the `hbFieldMaker`. Since the output file from `hbFieldMaker` only contains information for the drive gear, all nodes are being duplicated into a slave gear, continuously begins the iterative process to match the nodes from the mesh, with the nodes from the the `hbFieldMaker` output file. The reason why the nodes has to be duplicated into slave nodes are because the slave gear rotates in the opposite direction compared to the drive gear.

The iterative process are basically very simple, it takes the first  $(x, y)$  from the mesh and matches it with the closest  $(x, y, hb_b)$  from the `hbFieldMaker` output file by comparing the distances between the nodes and then moves on to the next mesh node. The  $h_b$ -value of the matched input file, Figure 3.11, will be assigned as the value for the corresponding gear profile field,  $h_b$ . This process is repeated for all nodes on the mesh, which finally gives a complete  $h_b$ -field. Worth to notice, it was found out that the amount of node points generated by the `hbFieldMaker` strongly influenced the accuracy of the  $h_b$ -field used by the OpenFOAM solver. Too few nodes were shown to give a very poor  $h_b$ -field, which is the reason why refinements had to be implemented in the `hbFieldMaker`, as explained in Section 3.3.2. The total amount of nodes generated by `hbFieldMaker` differed between  $1.2e6$  to  $2.5e6$ . These nodes were matched to a mesh consisted of  $0.6e5$ - $1.5e5$  cells. By giving this information it is easier to understand how time consuming the process becomes when the amount of nodes increases. Worst case scenario in this case would be to match a mesh with  $1.5e5$  cells with an output file containing  $2.5e6$  nodes, i.e  $1.5e5^{2.5e6}$  iterations. The distances between the the mesh nodes had to be compared to all nodes on the `hbFieldMaker` file to ensure that the correct value was assigned to the  $h_b$ -field. By then dividing the field according to their position on the gear, Figure 3.11, the savings in time becomes significant. A complete gear profile splitted in 8 pieces results henceforth with  $8 * 1.5e5^{\frac{2.5e6}{8}}$  iterations.

The above described matching process had to be repeated 30 times, one time for each mesh in the case-folder. The importance of keeping track of the nodes when the mesh was rotating became obvious. Correct node had to be matched with the correct value. For the mesh at angular position 1, the driver gear was rotating  $1^\circ$  in clockwise direction and the slave gear  $1^\circ$  in counter clockwise direction. Since the output file from the `hbFieldMaker` contained a mesh splitted according to Figure 3.11, i.e  $0^\circ - 45^\circ \dots 315^\circ - 360^\circ$  this had to be taken into consideration when the mesh was rotating. This was solved by rotating the `hbFieldMaker` nodes to the same angular position as the mesh before the actual searching algorithm could begin.

Since OpenFOAM uses both cell faces and patch faces, the above described procedure had to be repeated for all cell faces and patch faces. The only difference between the two procedures was that some of the patches had to be excluded from the matching process, i.e those patches were assigned a  $h_b$ -value of 0. The affected patched were the HPR (high pressure relief, LPR (low pressure relief) and the drive and slave drain patches, DR and DN, described in Figure 3.6.

When the matching procedure was completely finished, the field was written to a `volScalarField`.

### 3.3.4 Numerical solver settings in OpenFOAM

The solver used in simulations is an in-house which takes advantage of OpenFOAMs libraries. It solves Reynolds equations, Equation 2.19, over a domain using the finite volume method.

The divergence and gradient terms are solved by using Gaussian discretization linearly, i.e by using central differencing. The laplacian term,  $-\nabla \left( \frac{\rho h^3}{12\mu} \nabla p \right)$ , are also solved by using Gaussian discretization but with a corrected scheme. The corrected addition are assumed to perform an explicit correction against non-orthogonality, details can be found in [18],[22].

The code solves the linear system of equations with an implementation of pre-conditioning conjugate gradient method. The pre-conditioner is supposed to increase the convergence rate where the conjugate gradient method is a iterative solution procedure[23]. The chosen pre-conditioner is DIC, diagonal incomplete-cholesky.

In cases where the micro motion of the gears are taken into account, i.e  $\frac{\partial h}{\partial t}$  is varying, the law of motion will be calculated with respect of balancing the forces for each instant time, due to changes in the micro motion. This procedure is iterative which means that the Reynolds equation needs to be solved several times to reach balance for each angular position[5].

### 3.3.5 Balancing procedure

A stable solution occurs when the forces in z-direction of the gap are balanced, at this moment, the changes on the sliding element becomes very small or equal to zero,  $\frac{\partial h}{\partial t} \rightarrow 0$ . When the forces are not equal, the sliding element has to change position, i.e the bushing moves and the generated gap force changes. This process is used to predict the tilt of bearings.

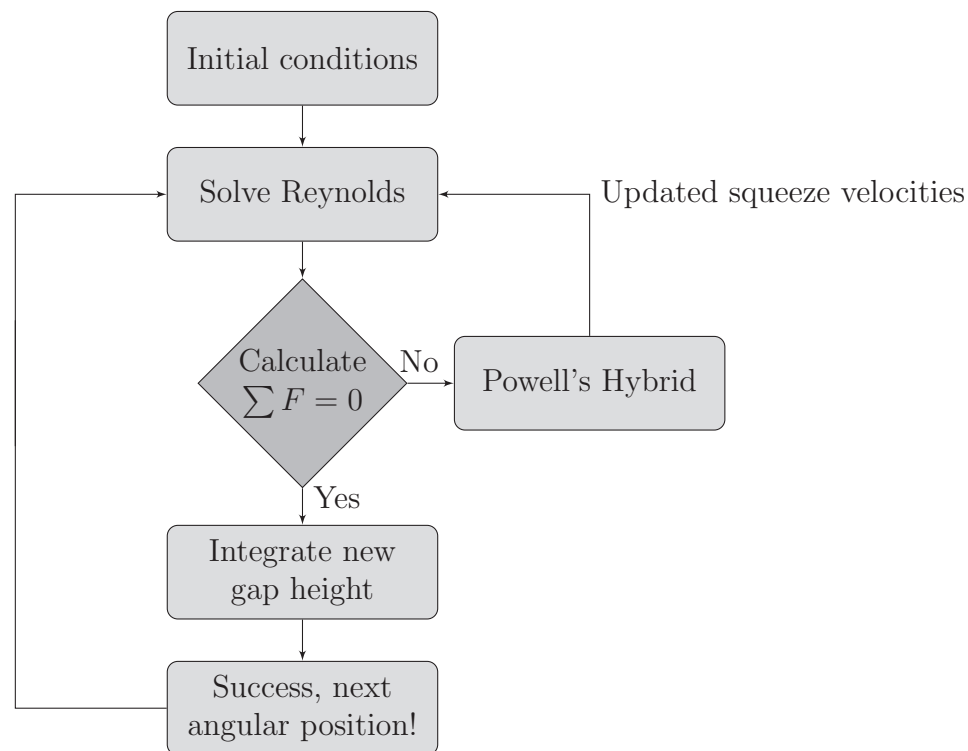


**Figure 3.12** – The schematic solver scheme to calculate the tilt of the bearing and the  $\sum F = 0$ .

In more details, the balancing of the bearing starts with assuming a gap height and the squeeze velocities as initial conditions. Then solving the Reynolds equation to find the gap force generated by the pressure distribution on the lubricating gap. The gap force is thereafter summed up with the other two forces acting in the same direction:

$$F_{axial} = F_{reliefgrooves} + F_{TSV} + F_{gap} \quad (3.2)$$

The force generated by the relief grooves and the force generated by the tooth space volumes are combined in OpenFOAM to one force, i.e the sum of the two forces. By knowing  $F_{axial}$  the forces acting in the three datum points, Figure 2.6, can be calculated together with the point of application, Equation 2.23. The point of application allows calculation of the moments acting on the three datum points. By comparing the  $F_{axial}$  with the  $F_{balance}$  the summation should end up zero, if not, the squeeze velocities has to be recalculated, Figure 3.12. The re-calculation of the squeeze velocities are performed by taking advantage of the open-source libraries from GSL[21], `gsl_multiroots.h`. to be able to find where the sum of forces is equal or close to zero.

The used library, named Multidimensional Root-Finding, is used to find the roots of a nonlinear system. By providing the chosen solver, Powell's Hybrid, one force equation, Equation 2.21, and two equations of moment, Equation 3.3 and Equation 3.4, where  $x_r$  and  $y_r$  in the equations are equal to the point of application, the solver could calculate a new set of squeeze velocities.

$$M_x = F_{axial}(y_r - y_{balance}) \quad (3.3)$$

$$M_y = F_{axial}(x_r - x_{balance}) \quad (3.4)$$

The new squeeze velocities are used to solve the Reynolds equation again and the procedure is repeated until the Powell's Hybrid solver predicts squeeze velocities that are within an acceptable range of a resultant force of zero. How close the solver will be to a resultant force of zero is decided by the pre-set residual and the step size in which the solver searches for the roots of the equations.

When the solver is as close as it can get to a balanced bushing, the simulation quits the GSL solver, integrates the squeeze velocities according to the time step. The result is then new predicted h values on the three datum points, Figure 2.6. These values are then used as initial conditions for the next time step and mesh, continuously the above described procedure has to be repeated, Figure 3.12.

It was found out during the project that when a chamfer was added to the system, the solver acted very instable and often crashed due to huge generated pressure distributions. The problem occurred since the Powell's Hybrid solver had problems to find a solution within the pre-set criterion. A solution to this was to smoothly increase the accuracy at the root finding solver and at the same time the gears lateral profile was slowly added to the system. This kept the generated pressure peaks and instability problems down to an acceptable level and the solver was able to continue to iterate.

The initial step size used by the solver was  $1e-6$ , this means that the solver changes the  $\frac{\partial h}{\partial t}$  value by  $1e-6$  each iteration in order to find a solution that gives a good prediction of the gap force. The criteria if the gap force was accepted or not (the residual) was initially set to  $1e-3$ . This means that the summation of the forces according to Equation 2.21 are accepted when the summation ended up within  $\pm 1e-3$  N. Since it occurred problem due to the given initial values a smoothing function was implemented both for the value of the step-size and the residual, both dependent on the number of iterations. The step-size was changed from  $1e-6$  to the variable step-size:

```
int cc;
cc = pgap -> progAngle; //Step-size according to iteration
double delta;
if(cc < 50){
    delta = 1e-3; //Step-size iteration 0 - 49
}
if(cc < 50 && cc >= 150){
```

```

        delta = 0.5e-3;          //Step-size iteration 50 - 149
    }
    if(cc < 150 && cc >= 1000){
        delta = 1e-4;          //Step-size iteration 150 - 999
    }
    if(cc >= 1000){
        delta = 1e-6;          //Step-size iteration 1000 - inf
    }

    gsl_vector* v = gsl_vector_alloc (3);
    gsl_vector* dF1 = gsl_vector_alloc (3);
    gsl_vector* dF0 = gsl_vector_alloc (3);

    for(int j=0; j<3; j++) {
        for(int k = 0; k < 3; k++) {
            if(k == j)
                //Calc new dh/dt
                gsl_vector_set(v,k, gsl_vector_get(x,k) + delta);
            else
                gsl_vector_set(v,k, gsl_vector_get(x,k));
        }
        ...
        ...
    }
    return GSL_SUCCESS;

```

The accepted value from the summation of the forces were also changes to give a more stable solution from the initial value of  $1e - 3$  N to:

```

do {
    iter++;
    status = gsl_multiroot_fdfsolver_iterate (s);
    printState (iter , s);

    if (status)
        break;
    if(cc < 500){
        //Acceptable error after summation of forces , 10 N
        // Iteration 0 - 499
        status = gsl_multiroot_test_residual (s -> f, 10);
    }
    if(cc >= 500 && cc < 1000){
        //Acceptable error after summation of forces , 1 N
        // Iteration 500 - 999
        status = gsl_multiroot_test_residual (s -> f, 1);
    }
    if(cc >= 1000 && cc < 1500){
        //Acceptable error after summation of forces , 1e-2 N
        // Iteration 999 - 1499
        status = gsl_multiroot_test_residual (s -> f, 0.01);
    }
}

```

```

        if(cc >= 1500){a
            //Acceptable error after summation of forces , 1e-3 N
            // Iteration 1500 - inf
            status = gsl_multiroot_test_residual (s -> f, 0.001);
        }
    }
while (status == GSL_CONTINUE && iter < 1000);
...

```

As mentioned above, the field at the gears lateral profile was also smoothly added to the system to avoid instabilities. This was done by solving the Reynolds equation with a modification, dependent on the iteration:

```

if(progAngle <= 1000){
    hbAngle = progAngle;
}
if(progAngle > 1000){
    hbAngle = 1000;
}
lduMatrix::solverPerformance sp = solve
(
    - fvm::laplacian(pow( (*ht) -
        (*hb/(-(9/1000)*hbAngle+10))),3.0)/(12.0*(mu)),(*p))
    + ((0.50*(*Ugears))
        & (fvc::grad((*ht) -(*hb/(-(9/1000)*hbAngle+10))))))
    + ((*Ugears) & (fvc::grad((*hb/(-(9/1000)*hbAngle+10))))))
    + (((*ht)-(*hb/(-(9/1000)*hbAngle+10)))
        * (fvc::div(*Ugears/2)))
    + (*dhdt)
);

```

The function slowly and linearly adds the gears lateral profile (\*hb) to the solver. The field is completely added after 1000 iterations ((\*hb/(-(9/1000) \* 1000 + 10)) = \*hb) and at that point and above assumed to generate a stable simulation. hbAngle is by the if-loop prohibited to grow larger than 1000.

### 3.3.6 Separation of forces

The developed pressure in the lubricating gap is generated by several different physical effects. By separating them, Figure 3.13, it simplifies the collation of their influence on the lubricating gap. The main source of pressure generation is generated by the Poiseuille effects, Section 2.1.3. The reason to this arises from the fact that the pressure on the boundaries diffuses into the lubricating gap. The other pressures acting on the gap are pressures generated by hydrodynamic effects, i.e pressure generated in the gap due to the rotation of the gears and non-flat or tilted surfaces. The force generated by the hydrodynamic pressure could be seen as the sum of pressure generated by the physical wedge term, normal squeeze term and the translational squeeze term from the Reynolds equation, Equation 2.19.

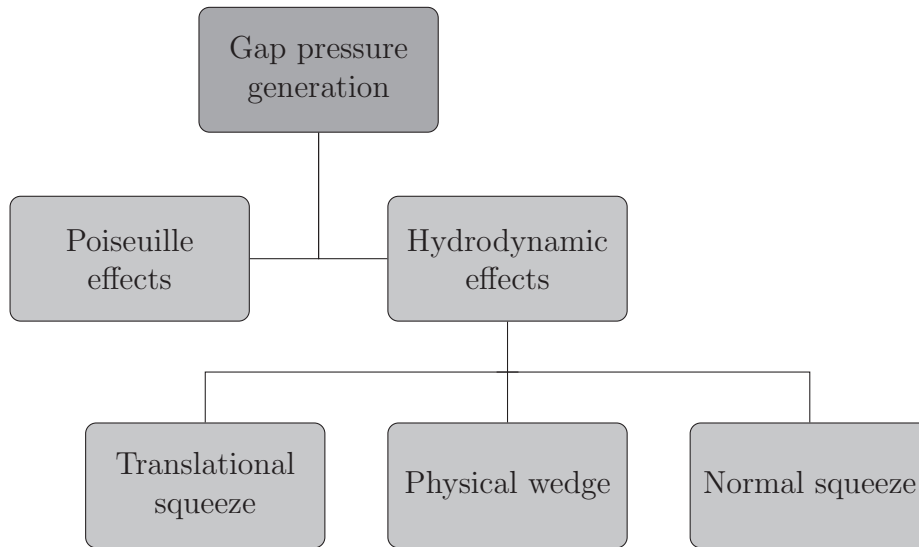


**Figure 3.13** – Separation of the pressure generative effects in the lubricating gap.

It is assumed that this work is the first work where the effects from the translational squeeze term are taken into consideration. Previous work such as [2], [3] and [5] assume a flat gear profile, i.e the gradient of  $h_b$  becomes zero and the term disappears. The translational squeeze due to the upper surface are neglected due to the fixed bearing, i.e zero velocity in flow direction.

Notice that a fixed gap height results in a neglected normal squeeze term since the squeeze velocities does not change in time. A chosen pre-given gap height makes the multi-root solver, Powell’s Hybrid, unnecessary and are therefore not solved, instead the solver only solves Reynolds equation and then moves on to the next angular position i.e next time-step. By using the solver with a fixed gap height position it simplifies the comparison and investigation between the different generated forces, a common approach to use, but without the balanced solution.

### 3.3.7 Leakage calculation

The leakages in the lubricating gap are calculated with respect to Equation 2.29 derived in Section 2.4. The leakages are summed up over specific sections of the gear, and presented separately to better understand the behavior of the leakages. The leakages are calculated at the tooth space volumes by following a tooth one cycle,  $360^\circ$ , by summing up the leakages to the drain and at last the leakages at the high pressure port and the low pressure port described in Figure 3.6. Leakages to the drain are represented by the summation of the leakages to the  $DR_d$  and  $DN_d$ . The leakages to the high pressure port and low pressure port are respectively calculated by the summation of leakages to  $HPR$  and  $LPR$ , all notations according to Figure 3.6.

The calculation of the leakages are performed at every angular position, since the angular position strongly influences the leakages.

### 3.3.8 Shear stress calculation and power losses

The shear stress is calculated in the solver by solving Equation 2.33 and Equation 2.35 and the power losses by solving Equation 2.38. The shear stress are assumed to me more or less unchanged during one cycle and are therefore only calculated for the first angular position of the mesh. It is implemented in OpenFOAM as a `volVectorField`, where the

specific shear stress for all cell centers are calculated as a vector consisting of the shear stress in x- and y-direction.

The power loss is the summation of the losses from all cells, calculated at different gap heights, rotational speeds and chamfers, but with a fixed pressure at 150 bar.

### 3.3.9 Initial conditions and geometry dimensions

The three datum point mentioned in Figure 2.6 are located according Table 3.1. The points originates from origo, described by Figure 2.6.

**Table 3.1** – Position of the datum plane points.

Point	x	y
$T_0$	0	-1.916960e-02 m
$T_1$	0	1.916960e-02 m
$T_2$	5.131960e-02 m	0

The initial conditions for the squeeze velocities are set according to Table 3.2. The initial

**Table 3.2** – Initial conditions for the squeeze velocities.

$\frac{\partial h}{\partial t}$	x
$\frac{\partial h_0}{\partial t}$	0
$\frac{\partial h_1}{\partial t}$	0
$\frac{\partial h_2}{\partial t}$	0

settings for the rotational speed were varied during the project since different rotational speeds were compared to each other. Used rotational speeds at specific simulation are presented together with the results. The viscosity,  $\mu$ , were assumed constant across the lubricating gap and therefore fixed to  $\mu = 0.0261$  Pa\*s according to the used oil, Shell Tellus Oil T46 at 50°.

Important geometrical properties had to be set as input data to the solver, Table 3.3.



**Table 3.3** – Pump geometrical properties. *POA = point of application*

Type	Name	Size
Teeth number	z	12
Gears diameter	d	0.03215 m
Drain diameter	Dd	0.020499 m
Outer diameter	Dout	0383392 m
High pressure groove area	HPGrooveArea	$80.78457e - 06 \text{ m}^2$
High pressure groove POA <sub>x</sub>	HPGrooveCMx	$16.075e - 03 \text{ m}$
High pressure groove POA <sub>y</sub>	HPGrooveCMy	$7.98946e - 03 \text{ m}$
Low pressure groove area	LPGrooveArea	$96.145681e - 06 \text{ m}^2$
Low pressure groove POA <sub>x</sub>	LPGrooveCMx	$16.075e - 03 \text{ m}$
Low pressure groove POA <sub>y</sub>	LPGrooveCMy	$-7.6689066e - 03 \text{ m}$
High pressure balance area	HPBalanceArea	$988.49049e - 06 \text{ m}^2$
High pressure balance POA <sub>x</sub>	HPBalanceCMx	$16.075e - 03 \text{ m}$
High pressure balance POA <sub>y</sub>	HPBalanceCMy	$4.7713e - 03 \text{ m}$
Low pressure balance area	LPBalanceArea	$549.03694e - 06 \text{ m}^2$
Low pressure balance POA <sub>x</sub>	LPBalanceCMx	$16.075e - 03 \text{ m}$
Low pressure balance POA <sub>y</sub>	LPBalanceCMy	$-8.5917552e - 03 \text{ m}$

Except for this, the solver needs to be provided with the boundary conditions, Figure 3.6, calculated by HYGESim. At last, the solver needs the file containing the  $h_b$ -field data, Section 3.3.3.

Note that, to be able to easier compare some of different results, the balancing part of the solver was excluded and the gap height was fixed to a constant value,  $10 \mu\text{m}$ . This specific gap height was chosen due to a previous investigation between experimental measured data and simulated data[2]. The results from their experimental are presented in Figure 3.14. Similar results are also found in previous previous work, [24], [11]. The result presented by [2] shows that the an increase gap height increases the leakages, as expected, but also that a gap height of  $10 \mu\text{m}$  gives a good agreement to the experimental data.

The different chamfers that were compared had a shape that followed the equation of a circle, Equation 3.5. This assumption was assumed to mimic a real chamfer.

$$r^2 = x^2 + y^2 \quad (3.5)$$

Three different chamfers were mainly compared during the project, their appearance are described by Figure 3.15.

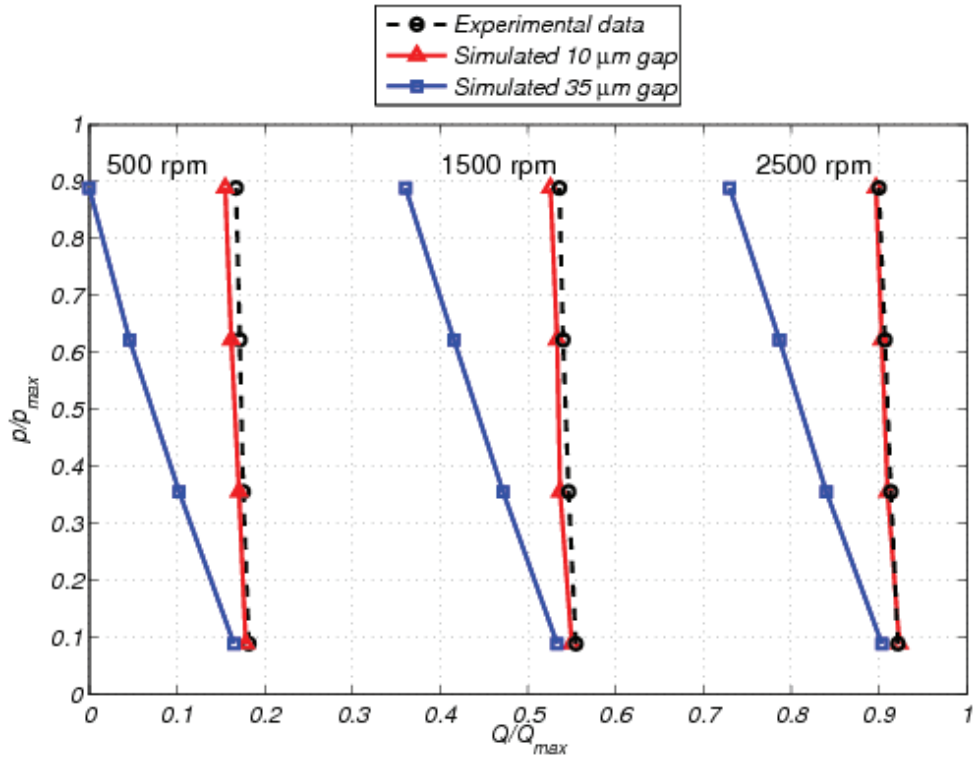


**Figure 3.14** – Pump characterization curves for varying gap heights, compared with experimental data[2].

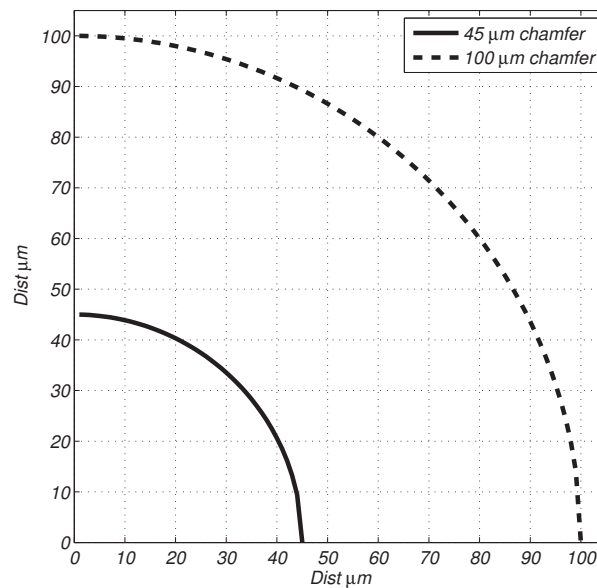


**Figure 3.15** – Different chamfers compared, assumed to follow the equation of a circle, Equation 3.5.

## 4 Results

All results pertain to the geometry, of the CASAPPA PLP20 11.2 Standard, 12 teeth pump.

The results will be presented with focus on comparing the changes in the lubricating gap depending on the implemented micro level surface features, the chamfer. First a qualitative comparison between the flow field with and without a chamfer. Then emphasizing the

effects on the different terms in the Reynolds equations. This follows by comparing how the leakage changes when a chamfer is added to the system according to the derivation in Section 2.4, which will include a comparison between different chamfers. The final part of the chapter presents results from a fully balanced simulation where the normal squeeze term are changed to get a balanced gear.

## 4.1 Pressure distribution and sources of hydrodynamic pressure generation

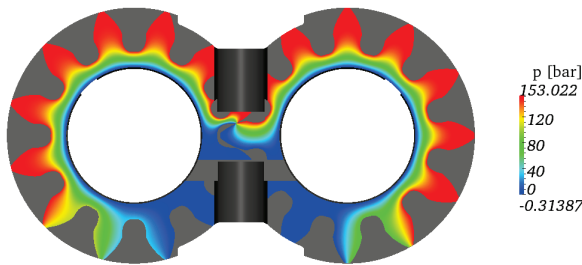


**Figure 4.1** – Pressure distribution without chamfer, fixed gap height of  $10 \mu m$  @ 150 bar, 1000 rpm.

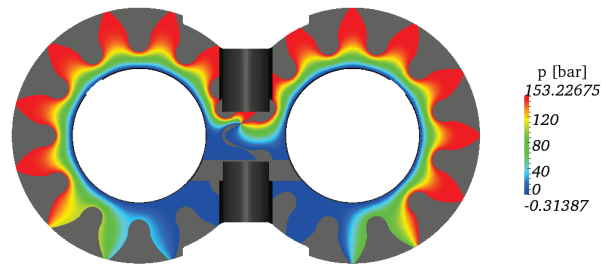


**Figure 4.2** – Pressure distribution with  $45 \mu m$  chamfer, fixed gap height of  $10 \mu m$  @ 150 bar, 1000 rpm.

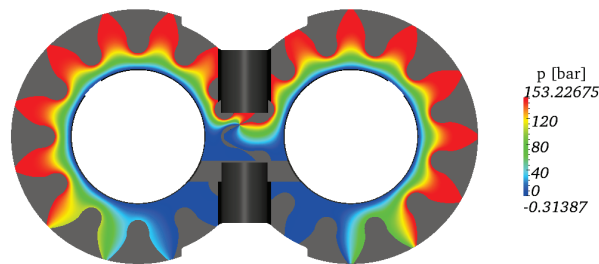


**Figure 4.3** – Pressure distribution with  $100 \mu m$  chamfer, fixed gap height of  $10 \mu m$  @ 150 bar, 1000 rpm.

A first look at the total pressure distribution, Figures 4.1, 4.2 and 4.3, indicate that at a fixed gap height gives no significant difference when comparing the case with and without a chamfer. The gap height are fixed to  $10 \mu m$  which also means that the normal squeeze term in the Reynolds equation ends up as zero.

The main source of pressure generation when considering a constant gap height is generated by the Poiseuille effect, the Poiseuille term is described in Section 2.1.3 and it is basically a diffusion term that diffuses the pressure from the boundaries, generated by HYGESim. Figures 4.4, 4.5 and 4.6 indicate that the pressure distribution generated by the Poiseuille effects is the main source of pressure generation in the gap with given setup.

The pressure distribution generated by the hydrodynamic effects is generated by the contribution from the translational squeeze term, physical wedge term and the normal squeeze term, Section 2.1.3. When the gap height is considered to be fixed the total pressure generation generated by the hydrodynamic effects is less than 1 % of the total pressure distribution. The hydrodynamic pressure distribution is plotted in Figures 4.7, 4.8 and 4.9. By separating the hydrodynamic pressure generation into the three included

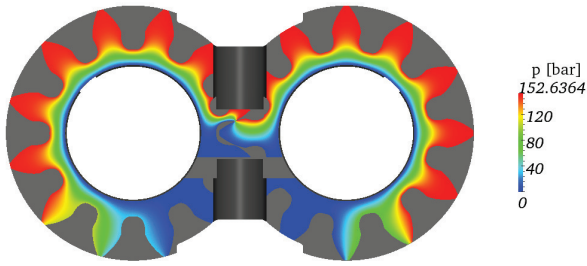


**Figure 4.4** – Pressure generation by the Poiseuille effects without chamfer, fixed gap height of  $10\ \mu\text{m}$  @ 150 bar, 1000 rpm.

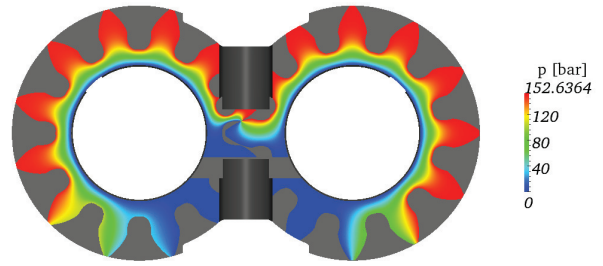


**Figure 4.5** – Pressure generation by the Poiseuille effects with a  $45\ \mu\text{m}$  chamfer, fixed gap height of  $10\ \mu\text{m}$  @ 150 bar, 1000 rpm.

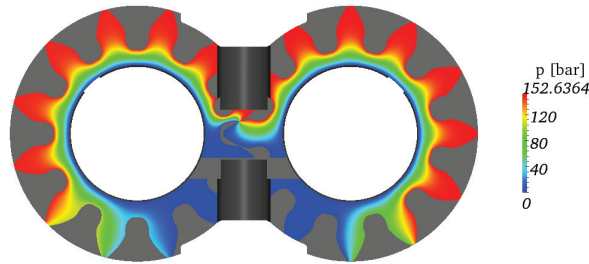


**Figure 4.6** – Pressure generation by the Poiseuille effects with a  $100\ \mu\text{m}$  chamfer, fixed gap height of  $10\ \mu\text{m}$  @ 150 bar, 1000 rpm.

terms, Figure 3.13, it is easier to get an understanding of the strength of the generative terms and the contribution to the total pressure generation inside the gap. As expected is the hydrodynamic pressure generation negligible when no chamfer is in use in the system and when the gap height is fixed, see Figure 4.7. Furthermore the biggest chamfer generates the largest hydrodynamic pressure,  $45\ \mu\text{m}$  and  $100\ \mu\text{m}$  chamfer.

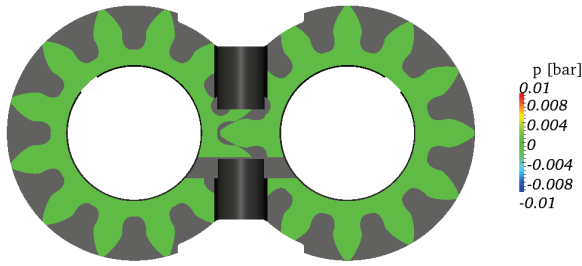
Note that, the total pressure generation could physically not become negative, the phenomena that then occurs is cavitation. The negative pressures plotted below does only occur when the terms are separated and investigated independently from each other.

The generated wedge effects are negligible when there is no chamfer, Figure 4.7. As mentioned in Section 2.1.3, the physical wedge term plays an important role when it comes to pressure generation in the lubricating gap, which is also proved by Figures 4.10, 4.11 and 4.12.

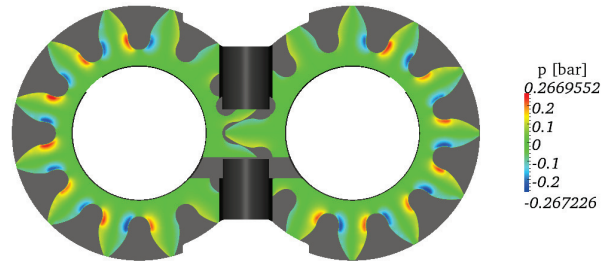
The physical wedge effects are assumed to increase with a decreased film thickness in the flow direction, Section 2.1.3. The figures over the hydrodynamic wedge effects could therefore easily be mistaken as incorrect. The low pressure regions occur before the high pressure region, according to the rotational direction of the gears. The underlying reason to this phenomena are better understood with a further investigation of the numerically solved terms. The wedge effect originates from the term:

$$\frac{u_{gears}}{2} \frac{\partial h}{\partial x_1} + \frac{u_{gears}}{2} \frac{\partial h}{\partial x_2} \quad (4.1)$$

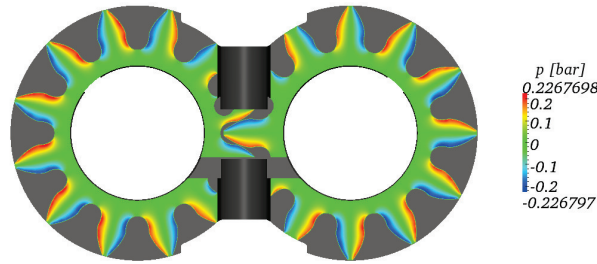
Since  $h$  is calculated as  $h = h_t - h_b$  the gap height after the subtraction will have the shape described by the top surface minus the chamfer. This are more detailed described in



**Figure 4.7** – Hydrodynamic pressure generation without chamfer, fixed gap height of  $10\ \mu\text{m}$  @ 150 bar, 1000 rpm.

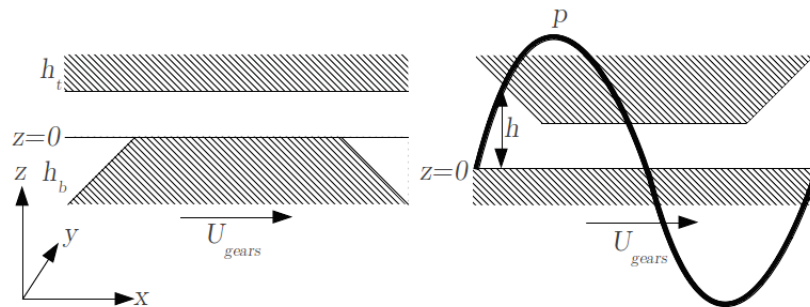


**Figure 4.8** – Hydrodynamic pressure generation with  $45\ \mu\text{m}$  chamfer, fixed gap height of  $10\ \mu\text{m}$  @ 150 bar, 1000 rpm.



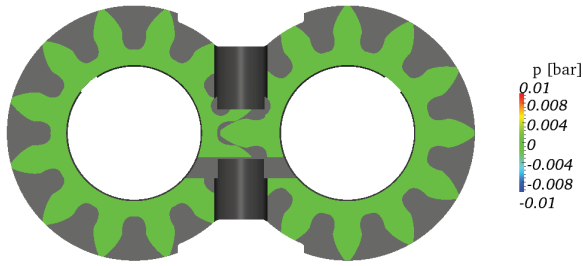
**Figure 4.9** – Hydrodynamic pressure generation with  $100\ \mu\text{m}$  chamfer, fixed gap height of  $10\ \mu\text{m}$  @ 150 bar, 1000 rpm.

Figure 4.13. By calculating the gap height  $h$ , and letting the bottom surface  $h_b$  rotate with the rotational speed of  $U_{gears}$  the high pressure region will occur according to the received result



**Figure 4.13** – Gap height  $h$  according to the solved equation, Equation 3.1.

The interesting term to compare is the translational squeeze term, as mentioned in Section 3.3.6. This work presents a study where additional things are taken into account in the Reynolds equation compared to previous works, such as the gradient that occurs on the gears lateral side. The translational squeeze term is according to Figures 4.14, 4.15 and 4.16 a good source of hydrodynamic pressure generation. It indicates that the term is important. It could be discussed why the results for the translational squeeze effects are presented for a case without chamfer, Figure 4.14. The point is to prove that the term is negligible when the gears lateral profile is flat.



**Figure 4.10** – Hydrodynamic wedge effects without chamfer, fixed gap height of  $10 \mu\text{m}$  @ 150 bar, 1000 rpm.

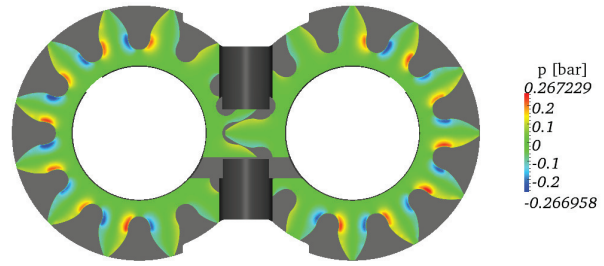


**Figure 4.11** – Hydrodynamic wedge effects with  $45 \mu\text{m}$  chamfer, fixed gap height of  $10 \mu\text{m}$  @ 150 bar, 1000 rpm.

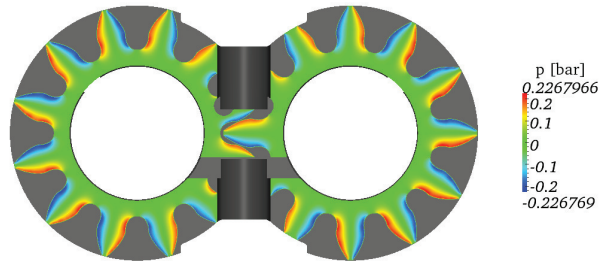


**Figure 4.12** – Hydrodynamic wedge effects with  $100 \mu\text{m}$  chamfer, fixed gap height of  $10 \mu\text{m}$  @ 150 bar, 1000 rpm.

Even if the physical wedge effects generates negative pressure in the rotational direction, the sum of the hydrodynamic pressure generation generates positive pressure in the rotational direction. In this case it is mainly due to the translational squeeze effects in the flow.

The stretch term, Equation 3.1 explained in Section 2.1.3, did not during the simulations show any tendency to influence the results. The term showed in all cases negligible effects and were therefore chosen not to be presented by separate figures.

In summary, all of the generated pressure arises from the Poiseuille term due to the boundary conditions from HYGESim. The hydrodynamic pressure generation represents less than 1% of the total pressure generated inside the gap but is still according to previous works, [2], [24] of significant importance when it comes to balancing the lubricating gap and the gear pump.

## 4.2 Leakage comparison

The leakages inside the lubricating gap is presented to give a better indication and understanding about the chamfers influence to the system and how the leakages changes according to a varying outlet pressure and rotational speed. All leakages are calculated with respect to Equation 2.29, derived in Section 2.4.

### 4.2.1 Leakage verification

To verify the leakage formulation derived earlier an assumption were made that a tiny chamfer added to the gears should have similar leakages as a case without a chamfer. Therefore a simple test case were set-up to verify the leakages. A chamfer of  $1\text{e-}9 \mu$

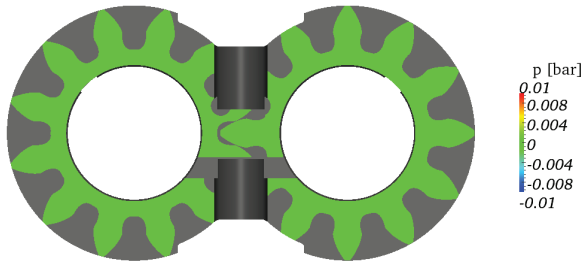


**Figure 4.14** – Translational squeeze effects without chamfer, fixed gap height of  $10\ \mu\text{m}$  @ 150 bar, 1000 rpm.

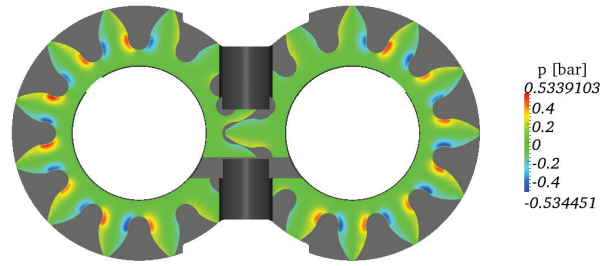


**Figure 4.15** – Translational squeeze effects with  $45\ \mu\text{m}$  chamfer, fixed gap height of  $10\ \mu\text{m}$  @ 150 bar, 1000 rpm.

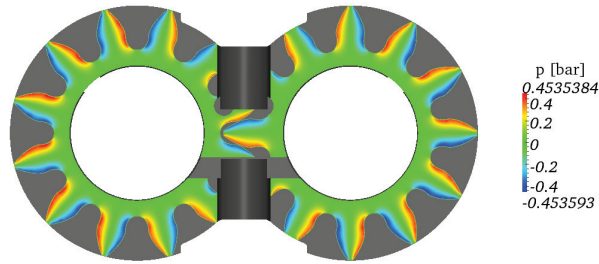


**Figure 4.16** – Translational squeeze effects with  $100\ \mu\text{m}$  chamfer, fixed gap height of  $10\ \mu\text{m}$  @ 150 bar, 1000 rpm.

was added to the gears lateral side and the result from the drain leakages is plotted in Figure 4.17. The result confirm that the leakage formulation are correctly derived and can therefore be used in the simulations.

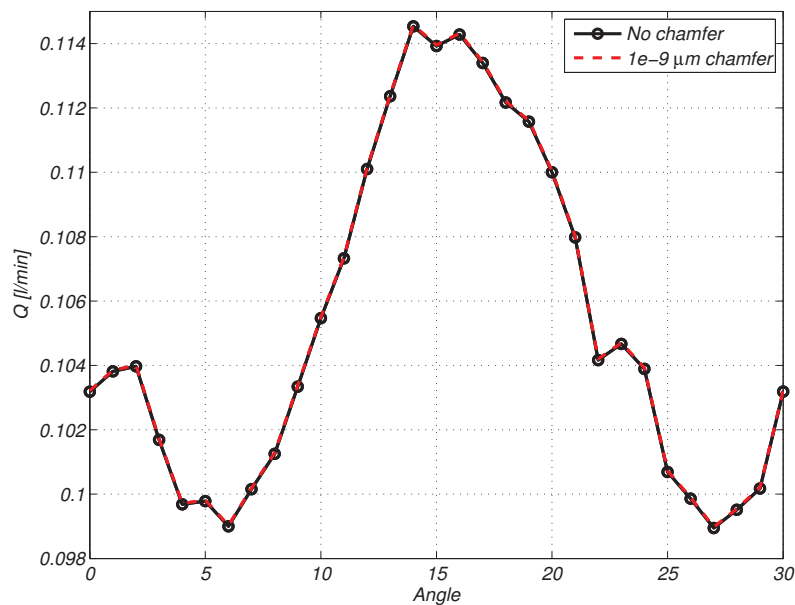


**Figure 4.17** – Leakage verification to the drain by comparing a tiny chamfer with a case without a chamfer.

## 4.2.2 Drain leakage comparison

The leakages to the drain are compared at different rpms and different pressures, in order to get a good understanding of the leakage behavior when adding a chamfer to the system. The drain leakages are only plotted at its first 30°. The reason for this is that the leakages show a repetitive tendency every 30°, this due to the 12 teeth on the gear.

According to Figures 4.18, 4.19, 4.20, and 4.21 the leakages when changing the pressure show a similar tendency, a larger chamfer decreases the leakages. A higher pressure tends also to increase the leakages and this can be explained by the increased influence from the pressure gradient caused by the diffusion from the boundaries. The differences in leakages between a pressure of 20 bar compared to a pressure of 240 bar are in a factor 10, from 0.013 to 0.16 l/min.

Notice that the pressure increase in these cases does not change the gap height. The gap height are kept constant at 10  $\mu\text{m}$ .

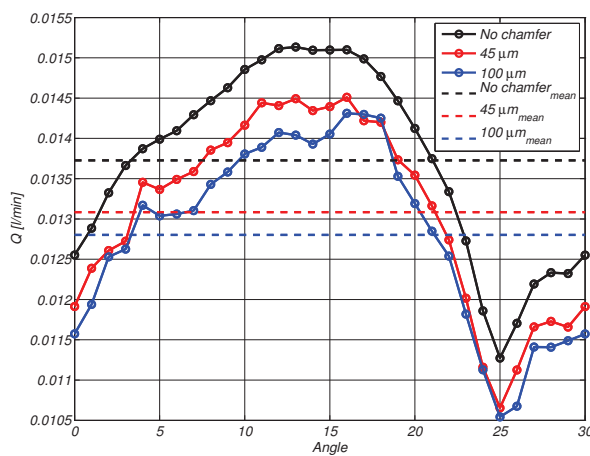


**Figure 4.18** – Leakages to the drain @ 20 bar, 1000 rpm.

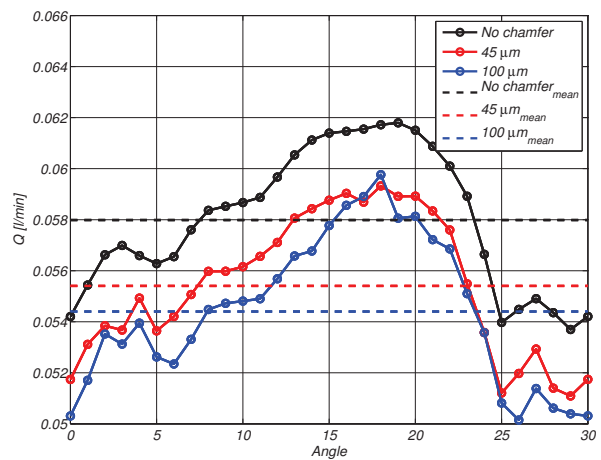


**Figure 4.19** – Leakages to the drain @ 80 bar, 1000 rpm.

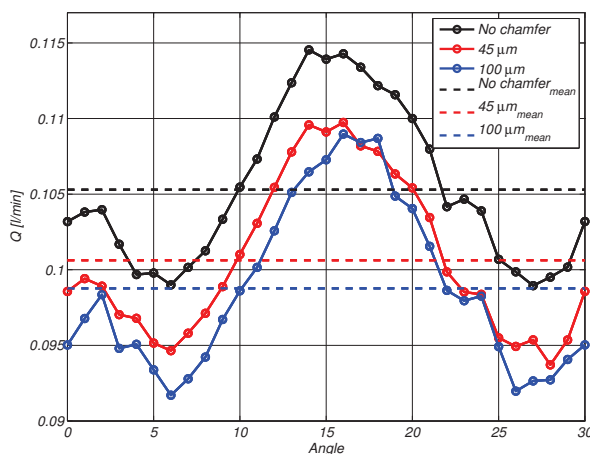


**Figure 4.20** – Leakages to the drain @ 150 bar, 1000 rpm.

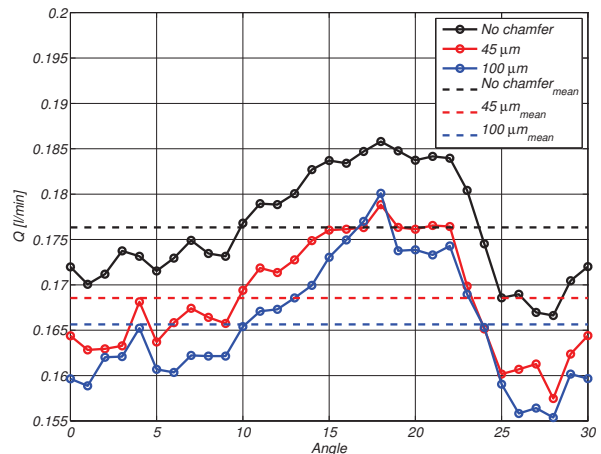


**Figure 4.21** – Leakages to the drain @ 240 bar, 1000 rpm.

The leakages to the drain at constant pressure with varying rotational speed show the tendency differ more at low rotational speed compared to high, according to the result in Figures 4.22, 4.23, 4.24 and 4.25. Nevertheless the trend is the same as when comparing different pressures, an increased chamfer decreases the leakages.



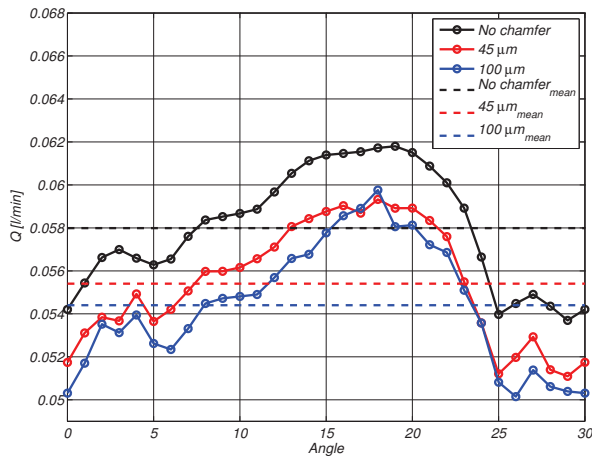


**Figure 4.22** – Leakages to the drain @ 150 bar, 200 rpm.

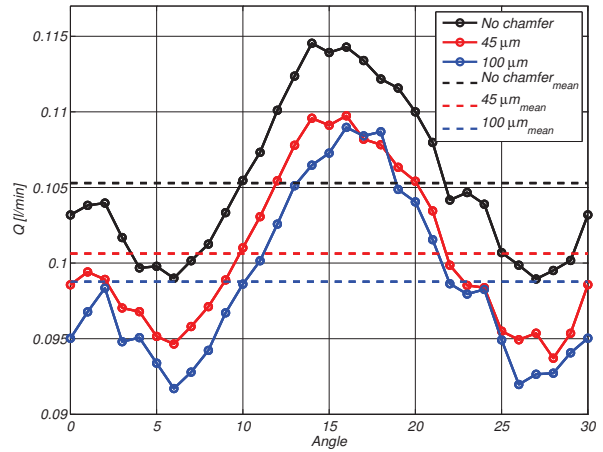


**Figure 4.23** – Leakages to the drain @ 150 bar, 1000 rpm.

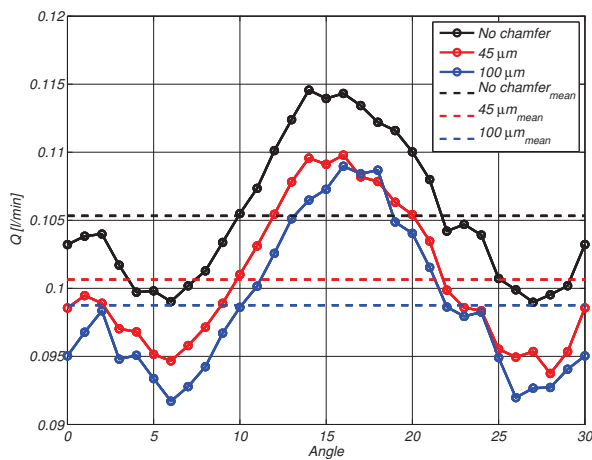


**Figure 4.24** – Leakages to the drain @ 150 bar, 1500 rpm.

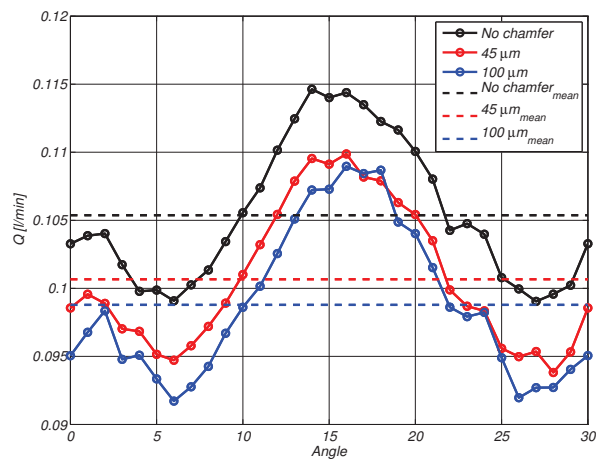


**Figure 4.25** – Leakages to the drain @ 150 bar, 2500 rpm.

### 4.3 Shear stress and power losses

The shear stresses acting on the gear are calculated by Equations 2.33 and 2.35, which means the shear stress is calculated at the gear side of the lubricating gap. The arrows in the Figures 4.26, 4.27 and 4.28 indicate the direction of the shear stress and an indication of the magnitude. The direction is dependent on the velocity and the pressure distribution found in the solved shear stress equations. The plotted surface shows the shear stress differences between 0 and  $60000 \frac{N}{m^2}$ .

It can be seen that the generated shear stress tends to increase with an increased chamfer. The red areas on the gear teeth increase which also the vector arrows tends to do since they represent the magnitude of the shear stress. By looking more on the direction of the shear stress it can be concluded that the shear stress on the tooth is mainly driven by the velocity term but pressure driven on the root of the tooth since the shear stress tends to point in the direction to the drain.

The largest shear stress is found in the region where the teeth interact with each other and the delivery port, red areas. There is also an increased shear stress on the teeth that interacts with the high speed groove, Figure 3.8. By furthermore comparing the main location of the shear stress between with and without a chamfer it can be seen that without

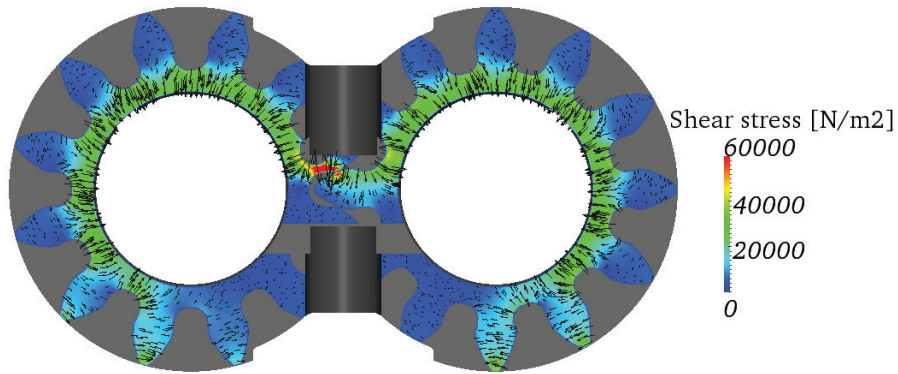


**Figure 4.26** – Shear stresses generated without chamfer, fixed gap height of  $10\ \mu\text{m}$  @ 150 bar, 1000 rpm.

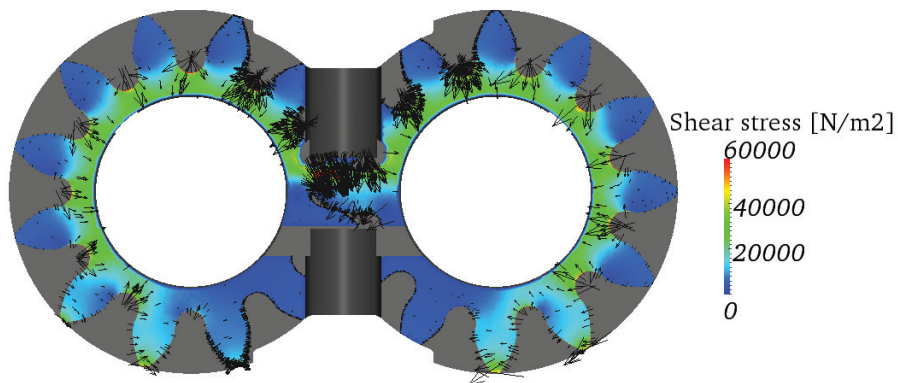


**Figure 4.27** – Shear stresses generated with  $45\ \mu\text{m}$  chamfer, fixed gap height of  $10\ \mu\text{m}$  @ 150 bar, 1000 rpm.

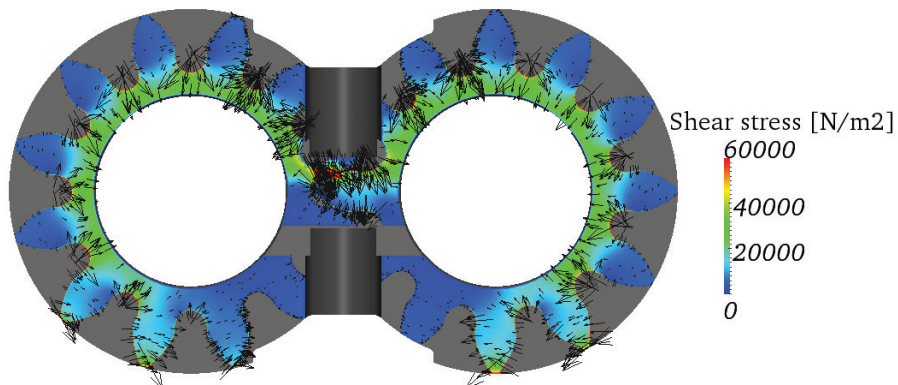


**Figure 4.28** – Shear stresses generated with  $100\ \mu\text{m}$  chamfer, fixed gap height of  $10\ \mu\text{m}$  @ 150 bar, 1000 rpm.

a chamfer the shear stress is constant over the gear surface, but with a chamfer on the gear teeth, the shear stress tends to be developed mainly on the edges of the gear. This can be seen more in Figures 4.29, 4.30 and 4.31 that show a zoom over the upper teeth of the gear.

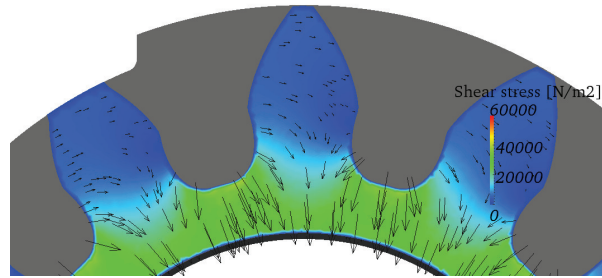


**Figure 4.29** – Shear stresses generated without chamfer with a zoom on teeth, fixed gap height of  $10\ \mu\text{m}$  @ 150 bar, 1000 rpm.

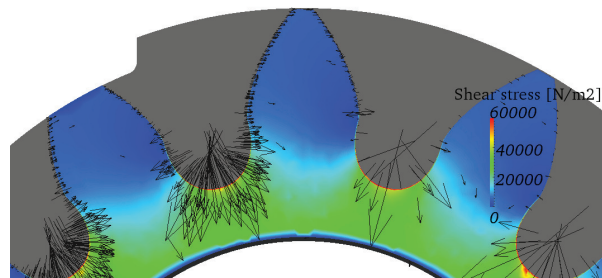


**Figure 4.30** – Shear stresses generated with  $45\ \mu\text{m}$  chamfer with a zoom on teeth, fixed gap height of  $10\ \mu\text{m}$  @ 150 bar, 1000 rpm.

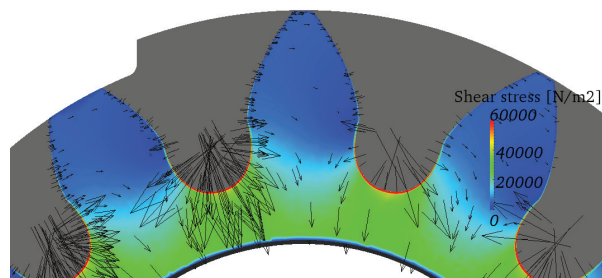


**Figure 4.31** – Shear stresses generated with  $100\ \mu\text{m}$  chamfer with a zoom on teeth, fixed gap height of  $10\ \mu\text{m}$  @ 150 bar, 1000 rpm.

Furthermore the viscous shear stress is a source for the generated power losses inside the lubricating gap. The power losses inside the gap are calculated with respect to Equation 2.38 at a range of different rotational speeds and gap heights. The values were mapped into a field which is presented to get good view over the losses at different operation conditions. At all data conditions, the gap height were set to constant, i.e no tilt were taken into account.

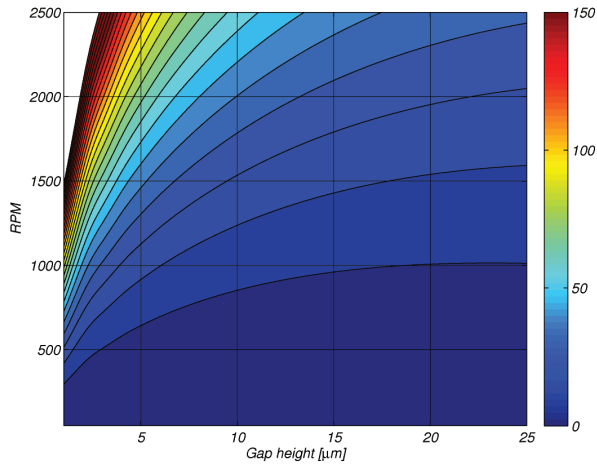


**Figure 4.32** – Power losses generated in the lubricating gap without chamfer, power losses,  $P$ , in  $W$ , constant gap height.

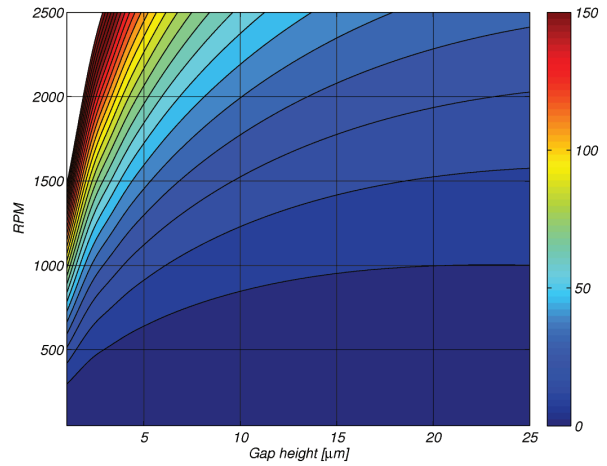


**Figure 4.33** – Power losses generated in the lubricating gap with  $45 \mu m$  chamfer,  $P$ , in  $W$ , constant gap height.

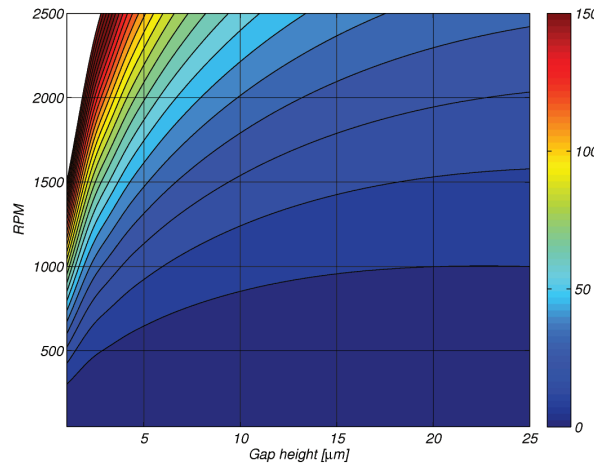


**Figure 4.34** – Power losses generated in the lubricating gap with  $100 \mu m$  chamfer,  $P$ , in  $W$ , constant gap height.

The power losses follow a predicted behavior, an increased rotational speed follows by increased losses and an increase gap height follows by decreased losses, Figures 4.32, 4.33, and 4.34. The reason for the increase in losses due to higher rotational speed could be explained by Equations 2.33 and 2.35. The velocity term (second part in the equations) increases, which produces more viscous shear.

The decrease in losses due to increased gap height occurs due to the decrease in pressure gradient inside the gap which means that the pressure generative term in the solved equations decreases. Highest amount of losses occurs in the case where the rotational speed is high and the gap height is small. Similar trends are found in previous work [2].

In all setups the energy losses are very low at rotational speeds below 1000 to 1500 and a gap height bigger than  $10 \mu m$ . At smaller gap heights increases the losses slightly, same effects occurs when the rotational speed increases.

How large the absolute difference in power losses is between the two different chamfers are presented in Figures 4.35 and 4.36. The power losses are in both cases compared to the case without a chamfer to give a realistic comparison. When looking at the results, it is interesting to verify that the differences between the two chamfers at different operative

conditions increases when the chamfer increases. Even if the differences tends to increase with the size of the chamfer the difference itself can be considered low. Just a couple of watts in difference which makes it in some perspectives more interesting to present the differences in percent. The two chamfers are in the same way compared with the case without a chamfer in Figures 4.37 and 4.38. Notice that the 45  $\mu\text{m}$  chamfer decreases the losses slightly at all operative conditions compared to the 100  $\mu\text{m}$  that tends to increase the losses at low gap heights and decrease it at large gap heights. The difference in percent also gives an indication that the differences tends to be larger at small gap heights almost independently of the rotational speed. Also large differences at low rotational speeds ( $<100$  rpm).

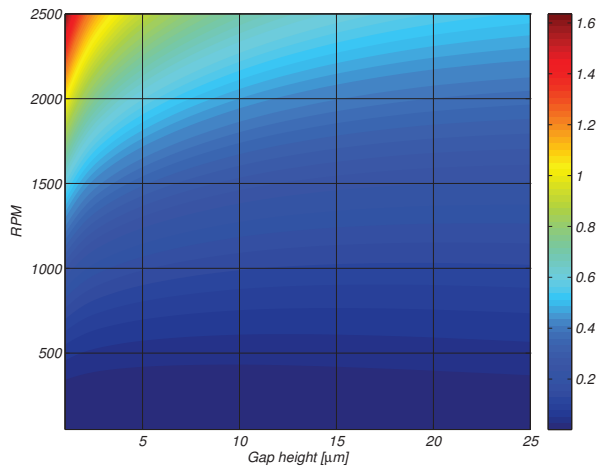


**Figure 4.35** – Absolute difference in power losses between without and with a 45  $\mu\text{m}$  chamfer, P, in W, constant gap height.

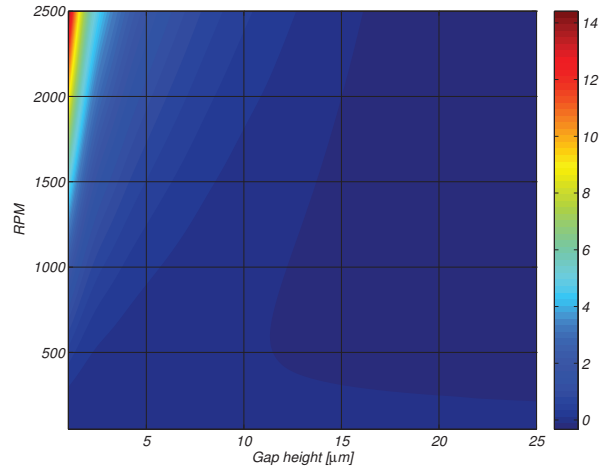


**Figure 4.36** – Absolute difference in power losses between without and with a 100  $\mu\text{m}$  chamfer, P, in W, constant gap height.

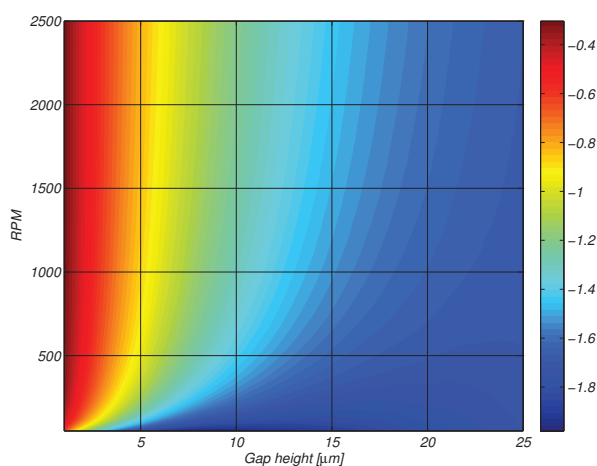


**Figure 4.37** – Difference in power losses between without and with a 45  $\mu\text{m}$  chamfer, P, in %, constant gap height.

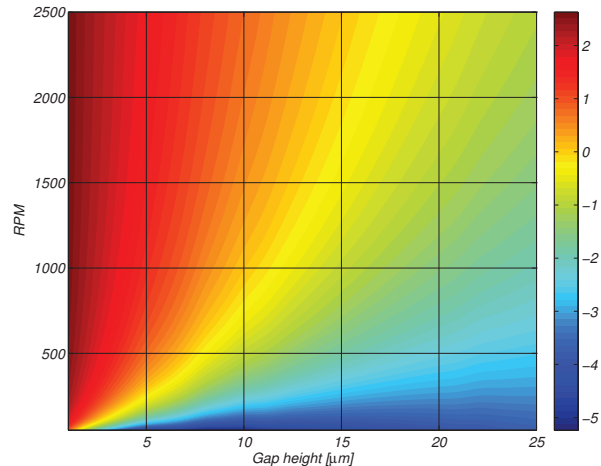


**Figure 4.38** – Difference in power losses between without and with a 100  $\mu\text{m}$  chamfer, P, in %, constant gap height.

The differences in percent at some specific operative conditions are presented in Table 4.1.

**Table 4.1** – Difference in pump losses at a given operating condition compared to the case without a chamfer. The case without a chamfer are assumed to be 1.0 and a value below indicates decreased power losses and vice versa.

		No chamfer	45 $\mu m$	100 $\mu m$
500 rpm	5 $\mu m$	1.0	0.990	1.008
	10 $\mu m$	1.0	0.986	0.991
	15 $\mu m$	1.0	0.984	0.982
1000 rpm	5 $\mu m$	1.0	0.991	1.013
	10 $\mu m$	1.0	0.987	1.001
	15 $\mu m$	1.0	0.985	0.992
1500 rpm	5 $\mu m$	1.0	0.992	1.015
	10 $\mu m$	1.0	0.985	1.005
	15 $\mu m$	1.0	0.984	0.996
2000 rpm	5 $\mu m$	1.0	0.992	1.016
	10 $\mu m$	1.0	0.988	1.007
	15 $\mu m$	1.0	0.985	0.999

#### 4.4 Pressure distribution generated by fully balanced gear

A stable solution and a fully balanced gear are defined by a system in equilibrium, and when the sum of the moments and the forces acting on the bushing is zero. The procedure how the equations are being balances and how the forces change are described in Section 3.3.5. The differences between a fully balanced gear with and without a chamfer are presented in a similar way as in Section 4.1, with the differences between the terms in the Reynolds equation.

The total pressure distribution generated by the balanced gear are presented in Figures 4.39 and 4.39. It is a noticeable difference when it comes to the maximum pressure generated inside the lubricating gap, 323 bar without a chamfer and 286 bar with a 45  $\mu m$  chamfer, a difference of approximately 37 bars. This gives a strong indication that the balanced gear is influenced by the chamfer.

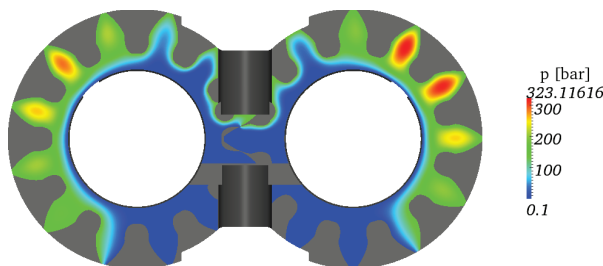


**Figure 4.39** – Pressure distribution without chamfer, balanced gear @ 150 bar, 1000 rpm.

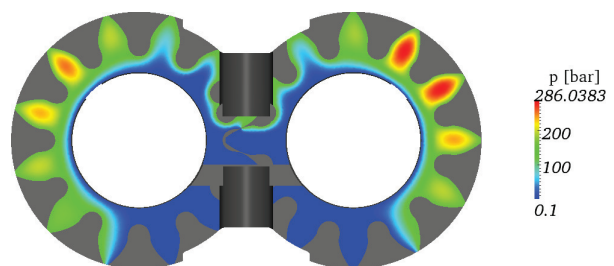


**Figure 4.40** – Pressure distribution with a 45  $\mu m$  chamfer, balanced gear @ 150 bar, 1000 rpm.

According to previous knowledge, the generated poiseuille effects are the same when comparing the two different cases, due to diffusion from the boundaries. Instead, the comparison is focused on the hydrodynamic pressure generation, the pressure generation that is developed to balance out the poiseuille effects.

By investigate further, the differences in hydrodynamic pressure generation, Figures 4.41 and 4.42, the tendency remains, the chamfer case generates lower maximum pressure. In addition to this, the effects from the hydrodynamic pressure generation are now much larger than 1 % of the total pressure generation, seen in Section 4.1. The reason for this is that the bearing has to be balanced and the only way to generate the amount of hydrodynamic pressure needed to balance the gears is to tilt the bearing block.

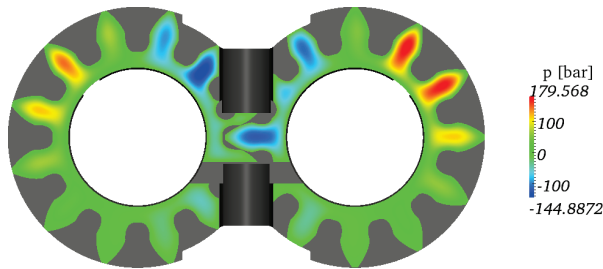


**Figure 4.41** – Hydrodynamic pressure generation without chamfer, balanced gear @ 150 bar, 1000 rpm.

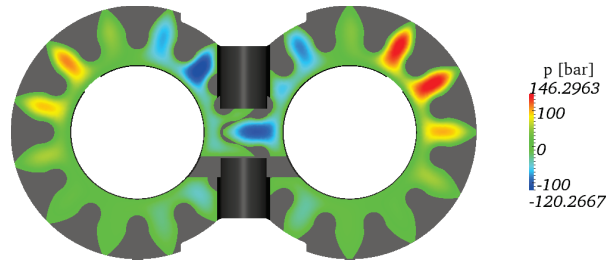


**Figure 4.42** – Hydrodynamic pressure generation with a 45  $\mu\text{m}$  chamfer, balanced gear @ 150 bar, 1000 rpm.

The effects generated by the different contributions to the hydrodynamic force are presented below. The effects generated by the normal squeeze should end up zero when the gear is balanced, and this is not seen in the following figures, Figures 4.43 and 4.44. The reason for this is that the presented result is only plotted at one instantaneous position. When summing the contribution over a complete revolution, the normal squeeze effects does end up as zero.

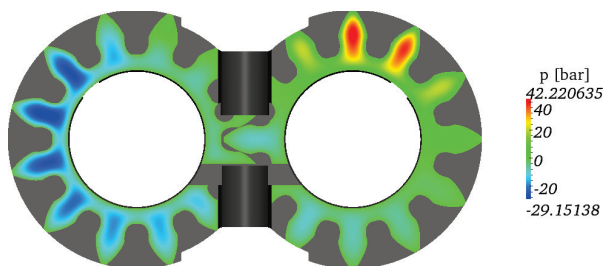


**Figure 4.43** – Normal squeeze pressure generation without chamfer, balanced gear @ 150 bar, 1000 rpm.

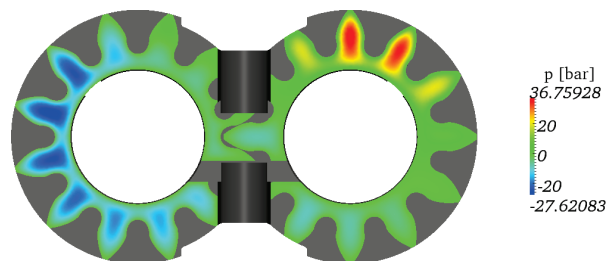


**Figure 4.44** – Normal squeeze pressure generation with a 45  $\mu\text{m}$  chamfer, balanced gear @ 150 bar, 1000 rpm.

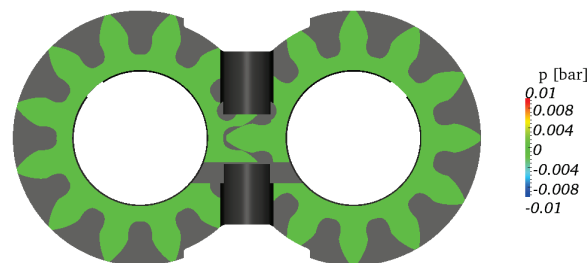


**Figure 4.45** – Translational squeeze pressure generation without chamfer, balanced gear @ 150 bar, 1000 rpm.

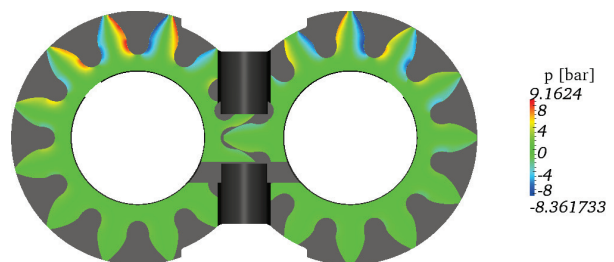


**Figure 4.46** – Translational squeeze pressure generation with a 45  $\mu\text{m}$  chamfer, balanced gear @ 150 bar, 1000 rpm.

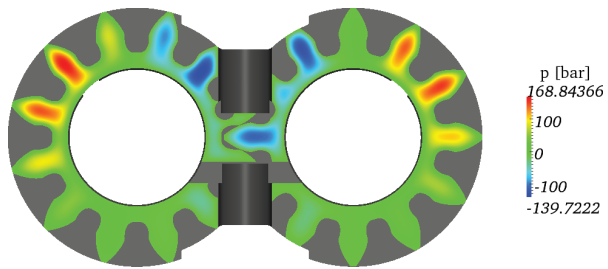


**Figure 4.47** – Physical wedge pressure generation without chamfer, balanced gear @ 150 bar, 1000 rpm.

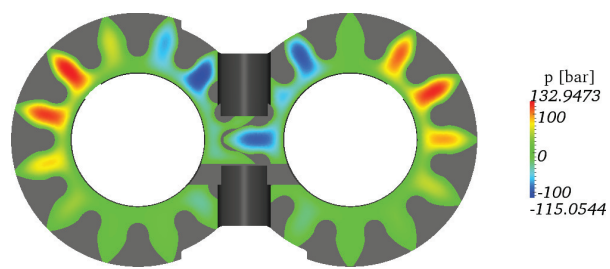


**Figure 4.48** – Physical wedge pressure generation with a 45  $\mu\text{m}$  chamfer, balanced gear @ 150 bar, 1000 rpm.

The main difference occurs when comparing the physical wedge and the translational squeeze effects. The translational squeeze effects are zero without a chamfer, Figure 4.45, because the gradient on the gears lateral side ends up zero,  $u_{gears} \frac{\partial h_b}{\partial x_1} + u_{gears} \frac{\partial h_b}{\partial x_2}$ . The reason is that the case with a chamfer contains a gradient the contribution by the translational squeeze becomes significant, Figure 4.46.

The physical wedge, presented in Figures 4.47 and 4.48, is the main source when it comes to generate hydrodynamic pressure. The case without a chamfer generated almost 36 bars higher maximum pressure compared to the case with a 45  $\mu\text{m}$  and it is here the difference between with and without a chamfer originates. The contribution generated by the translational squeeze is a factor 10 lower than the contribution from the physical wedge when comparing the maximum pressure difference.

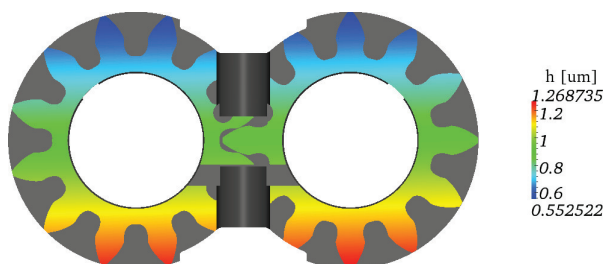


**Figure 4.49** – Tilt of bearing without chamfer, balanced gear @ 150 bar, 1000 rpm.

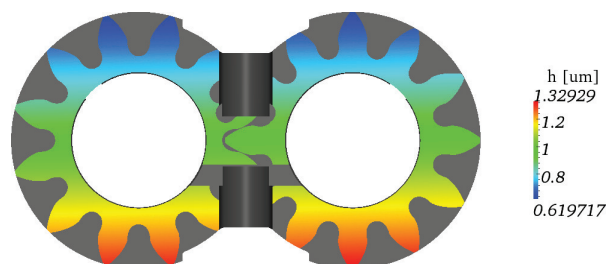


**Figure 4.50** – Tilt of bearing with a 45  $\mu\text{m}$  chamfer, balanced gear @ 150 bar, 1000 rpm.

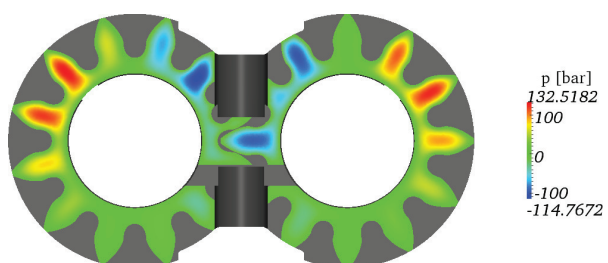


**Figure 4.51** – Separated physical wedge term showing pressure generation due to tilt @ 150 bar, 1000 rpm.

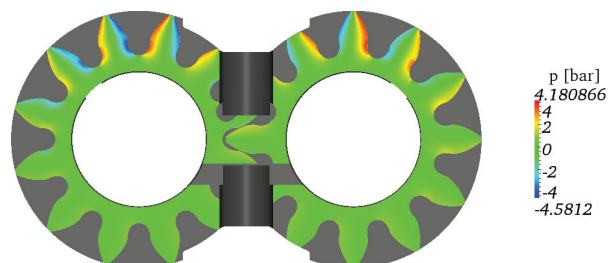


**Figure 4.52** – Separated physical wedge term showing pressure generation due to chamfer @ 150 bar, 1000 rpm.

In the end, it is interesting to investigate whether the contribution of the physical wedge originates from the tilt itself or from the chamfer. When looking at the case without a



chamfer, the physical wedge effects are only generated by the tilt of the bearing, Figure 4.49. When investigating the effects generated by a case with a chamfer, it can be seen that the tilt of the bearing is generated both by the chamfer, and the tilt. This can be explained by studying the physical wedge term in more detail, Equation 4.2, where  $h = h_t - h_b$ .

$$\frac{u_b}{2} \frac{\partial h}{\partial x_1} + \frac{u_b}{2} \frac{\partial h}{\partial x_2} = \frac{u_b}{2} \frac{\partial (h_t - h_b)}{\partial x_1} + \frac{u_b}{2} \frac{\partial (h_t - h_b)}{\partial x_2} \quad (4.2)$$

The effect generated by the tilt of the bearing are caused by the  $h_t$ -term and the effects by the chamfer by the  $h_b$ -term.

$$\frac{u_b}{2} \frac{\partial (h_t)}{\partial x_1} + \frac{u_b}{2} \frac{\partial (h_t)}{\partial x_2} \quad (4.3)$$

$$\frac{u_b}{2} \frac{\partial (-h_b)}{\partial x_1} + \frac{u_b}{2} \frac{\partial (-h_b)}{\partial x_2} \quad (4.4)$$

By separating the physical wedge terms the effects generated by tilt, Equation 4.3, and the chamfer, Equation 4.4, becomes visible. The resulting pressure generation are presented in Figures 4.51 and 4.52. It can clearly be seen that the pressure generation generated by the tilt of the bearing are larger than the generation by the tilt, therefore the tilt is the dominating factor when it comes to produce hydrodynamic pressure.

By studying the tilt itself it can be seen that the largest gap height occurs at the LP-port and that there is a slight difference between the two cases, Figures 4.49 and 4.50 in both maximum and minimum values. A common approach to define the tilt is by using the following formulation,  $t$ . This formulation is used in previous works such as [2], [24].

$$t = \frac{h_{max} - h_{min}}{2h_{avg}} \quad (4.5)$$

The tilt without a chamfer, Figure 4.51 are  $t = 0.394$  compared to the tilt with a  $45 \mu m$  chamfer,  $t = 0.366$ , i.e a smaller tilt with a chamfer.

## 5 Summary and Conclusions

The main concern of this study is to describe, predict and get a good understanding how micro level surface features influence the lubricating gap within external gear pumps. By using the open-source CFD software OpenFOAM and a in-house solver to solve Reynolds equation it is assumed to give an accurate and good prediction of the generated pressures, leakages and power losses.

The derived version of Reynolds equation in this thesis takes into account effects such as the translational squeeze on the gears lateral side. Since the effects generated by the gears shaped lateral side, the chamfer, a well-known procedure in the manufacturing process, it is of interest to get a better understanding of the reasons why it is used. The following summary and conclusions are therefore separated into two different parts, where the first part discuss the simulations involving a chamfer with a fixed gap height, leakages and at last power losses. The second part of the conclusion and discussion involves simulations regarding a complete balanced gear and the origin of the generated pressures.

## 5.1 Fixed gap height, leakages and powerlosses

By investigate the effects of a chamfer in a steady-state environment with a fixed gap height it has to be taken into considerations that huge simplifications are being made but it is still a good procedure to get a good understand of the differences between a case with a chamfer and without a chamfer.

By taking a first look at the hydrodynamic pressure generation, Figures 4.7, 4.8 and 4.9 a first indication and proof are shown that there is an effect by the chamfer, but its hard to tell how big the effects are when looking at the complete lubricating gap, it can only be concluded that there is some effects generated by the chamfer. This conclusions brings the discussion forward since it has to be mentioned that this is the first presented work where effects like this, micro level surface features are taken into account, which also is proved by the "new" effect, the translational squeeze effects. The translational squeeze effects is a pure result of the contribution generated by the chamfer, even if the generated pressure contribution are small compared to the total pressure generation, Figure 4.15.

It can also be concluded that the chamfer itself has a positive effect when it comes to the drain leakages. The drain leakages according to the result presented in Section 4.2.2 follows a similar behavior where a bigger chamfer tends to decrease the leakages. Even if the amount of decreased leakages are low, it is a sign and may also be an answer to why different manufacturers tends to put a chamfer on the gears lateral side. Basically, the results tells that the decrease in leakages exists at both high and low pressures as well as at high and low rotational speeds.

When it comes to the shear stresses it can be confirmed that an increased chamfers tends to increase the shear stresses, the differences can be quite hard to visualize but according to Figures 4.29, 4.30 and 4.31 can it be seen that the red area increases with increasing chamfer. When continuously looking at the power losses at different operating conditions the results give an interesting point of view. The losses tends to decrease with the 45  $\mu m$  chamfer compared to the 100  $\mu m$  chamfer. Even if the decrease is almost negligible at normal operative conditions its gives a significant contribution to the fact why a chamfer are used by the manufacturers. Have in mind that the 100  $\mu m$  in the normal operative conditions tends to increase the losses which contradicts that a chamfer itself would in all sizes and forms decrease the losses.

## 5.2 Fully balanced gear

According to the presented results in Section 4.4 are the differences between a gear profile with and without a chamfer quite small, but its still interesting that the case with a chamfer tends to generate a lower maximum pressure according to the without a chamfer, Figures 4.39 and 4.40. The reason for this can be explained by continuing to look at the separated terms in the Reynolds equation. It has already been concluded that the poiseuille effects are the same regardlessly if there is a fixed gap height, with or without a chamfer. The differences are mainly generated by the hydrodynamic effects and according to the results, especially the physical wedge. The differences between the two cases are here almost equal to the total pressure differences, i.e a difference of almost 37 bars.

The translational squeeze effects originates as mentioned before only due to the chamfer, but its contribution according to Figure 4.46 are small when putting the in comparison with the total pressure distribution. Nevertheless is the effects in such magnitude that they can not be neglected. The generated pressure contributes to the hydrodynamic pressure generation which in the end acts as a counteracting force to neutralize the forces acting on the bushing, Figure 2.2.

A deeper look into the contributions to the physical wedge, Equation 4.3 and Equation 4.4 concludes that the generated pressure to balance the gear are mainly caused by the tilt of the bushing and not the chamfer itself. Even though its interesting to have in mind that the chamfer tends to lower the value  $t$ , explained by Equation 4.5. The differences between the two  $t$  values are only 7.6% but nevertheless a difference that can be explain as an effect by the chamfer.

Finally, to summarize everything; the work has reached its aim to quantifying and proving the impact generated by a change in the micro geometrical level. It can be concluded that the chamfer itself by the given and presented results tends to influence the system, both positively and negatively. The effects are evaluated fairly and should therefore be considered.

- The effects by the translational squeeze and a negative pressure generation in the rotational direction by the physical wedge are a proven effects by the chamfer and proven by running simulations with a fixed gap height.
- A chamfer according to the fully balanced simulations increases the hydrodynamic pressure generation which gives an increasing and supporting effect to the balancing of the bushing. The tilt,  $t$ , and the maximum generated pressure are lower, as an effect by the chamfer, which has been proven as an positive effect since the need of a tilt to balance the gear decreases, which in the end can help avoiding wear. The contribution to the hydrodynamic forces are still mainly generated by the tilt, the chamfers are small in comparison.
- The leakages to the drain decreases in all of the tested conditions. Positive when it comes to avoid leakages but the differences are less than 1 % and may therefore be neglected.
- The power loss differences in percent generated between the gear and the bushing are proven to decrease with the 45  $\mu m$  and this behavior are changes when the chamfer is increased to a 100  $\mu m$  chamfer compared to a case without a chamfer. In both cases occurs the biggest differences at low rotational speeds even if the change itself are small and almost negligible.

## 6 Future work

The results in the presented study can be improved in several ways, excluded the different shapes and chamfer sizes of the gears lateral surface. The following recommendations for future works are proposed.

- Since the implementation of a micro level surface feature tends to be strongly mesh dependent an investigation regarding the presented results and how they depends on the mesh resolution.
- Find out an optimal chamfer size when it comes to terms of hydrodynamic pressure generation, leakages and power losses. Also try different types of micro level surfaces changes for example a linear profile on each tooth on the gears lateral side.
- Run simulations when deformation and variabel properties are taken into account.

Furthermore is it important to continue develop the tools used during the present study. Optimize and continued development of the hBFieldMaker is a demand to get better and faster implementation of the micro level surface features.

The linking procedure in OpenFOAM are time-consuming and slow, an implementation of a C++ tree library is a possible solution, such as ANN [25].

## References

- [1] J. Ivantysyn and M. Ivantysynova, *Hydrostatic Pumps and Motors*. New Dehli, India: Akademia Books International, first english ed., 2001.
- [2] A. Vacca, S. Dhar, and T. Oppwerwall, “A coupled lumped parameter and cfd approach for modeling external gear pumps,” *The Twelfth Scandinavian International Conference on Fluid Power*, May 18, 2011.
- [3] P. Casoli, A. Vacca, and G. Berta, “A numerical model for the simulation of flow in hydraulic external gear machines,” *PTMC2006 Power Transmission and Motion Control*, 2007.
- [4] N. D.Manring and S. B.Kasragadda, “The theoretical flow ripple of an external gear pump,” *ASME Journal of Dynamic Systems, Measurement, and Control*, vol. 125, pp. 396–404, 2003.
- [5] M. Zecchi, A. Vacca, and P. Casoli, “Numerical analysis of the lubricating gap between bushes and gears in external spur gear machines,” *Proceedings of FPMC 2010 Bath/ASME Symposium on Fluid Power and Motion Control*, 2008.
- [6] S. Falfari and P. Pelloni, “Model for simulating dynamic behavior of external gear pumps,” *Commercial Vehicle Engineering Congress & Exhibition*, October, 2007.
- [7] Z. B and B. M, “Modelling and simulation of external gear pumps and motors,” *5th FPNI PhD Symposium*, July, 2008.
- [8] A. Heisler, “The design of low-inertia, high-speed external gear pump/motors for hydrostatic dynamometer systems,” *SAE World Congress & Exhibition*, April, 2009.
- [9] W. Wustman, “Cfd-simulation of the reversing process in external gear pumps,” *6th Int. Fluid Power Conference*, Mars-April, 2008.
- [10] E. Ko and C. Hokke, “An experimental investigation into the design and performance of hydrostatically loaded floating wear plates in gear pumps,” *Wear*, vol. 209, pp. 184–192, 1997.
- [11] E. Ko, O. Kurban, and C. Hooke, “An analysis of the lubrication mechanisms of the bush-type bearings in high pressure pumps,” *Tribology International*, vol. 30, pp. 553–560, 1997.
- [12] M. Zecchi, “Reynolds equation in caspar,” *Report No: MAHA12-2010-IN*, 2010.
- [13] J. Shukla, S. Kumar, and P. Chandra, “Generalized reynolds equation with slip at bearing surfaces: Multiple-layer lubrication theory,” *Wear*, vol. 60, pp. 253–268, 1979.
- [14] B. O. Bernard J.Hamrock, Steven R.Schmid, *Fundamentals of Fluid Film Lubrication*. New York, NY: Marcel Dekker, Inc, second english ed., 2004.
- [15] I. A. of Manufacturing, T. C. in Fluid Power Equipment, and Components, *Hydraulics In Industrial and Mobile Applications*. Milano, Italy: assofluid, 2007.

- [16] Casappa, “Casappa - fluid power design.” <http://www.casappa.com/>.
- [17] Shell, “Shell tellus oil t46 properties.” [http://www.epc.shell.com/Docs/GPCDOC\\_X\\_cbe\\_24855\\_key\\_140002044283\\_6623.pdf](http://www.epc.shell.com/Docs/GPCDOC_X_cbe_24855_key_140002044283_6623.pdf).
- [18] OpenFOAM, “Openfoam®: Open source cfd.” <http://www.openfoam.com/>. Version 1.6.x.
- [19] Purdue, “Maha fluid power research center.” <https://engineering.purdue.edu/Maha/>.
- [20] C. Geuzaine and J.-F. Remacle, “Gmsh: a three-dimensional finite element mesh generator with built-in pre- and post-processing facilities.” <http://www.geuz.org/gmsh/>, Oct 15 2010. Version 2.5.0.
- [21] GSL, “Gsl - gnu scientific library.” <http://www.gnu.org/software/gsl/>, May 6 2011. Version 1.15.
- [22] H. Jasak, *Error Analysis and Estimation for the Finite Volume Method with Applications to Fluid Flows*. PhD thesis, University of London, London, 1996.
- [23] M. Hestens and E. Steifel, “Method of conjugate gradients for solving linear systems,” *Journal of Research*, p. 29:409–436, 1952.
- [24] M. Borghi, M. Milani, F. Paltrinieri, and B. Zardin, “Studying the axial balance of external gear pumps,” *SAE 2005 Commercial Vehicle Engineering Congress and Exhibition Rosemonde*, November, 2005.
- [25] D. M. Mount and S. Arya, “Ann: A library for approximate nearest neighbor searching.” <http://www.cs.umd.edu/~mount/ANN/>.